Chapter 8

Boundary Layer Turbulence Behavior

8.1 Introduction

In the previous chapter, we found that the classic arguments on inner and outer layer similarity hold well over a very large range of Reynolds numbers, and that the direct effects of compressibility on the mean flow appear to be rather small: the most notable differences between zero pressure gradient subsonic and supersonic boundary layers may be attributed to the variation in fluid properties across the layer. As we show, similar considerations apply to many aspects of the turbulence behavior. However, recent measurements have also indicated some interesting differences between turbulence in subsonic and supersonic boundary layers that do not seem to scale according to fluid property variations. Differences in turbulence length and velocity scales, and the structure of the large-scale, shear-stress-containing motions have been observed, which may indicate that the turbulence dynamics are affected at a lower fluctuating Mach number than previously believed.

"True" compressibility effects, beyond the effects determined by fluid property variations, are usually described in terms of a Mach number representative of the fluctuations. Several candidates were introduced in Chapter 4. It is also possible that some of these apparent changes in the turbulence structure are due to Reynolds number effects, rather than Mach number effects. As pointed out earlier, the characteristic Reynolds numbers encountered in high-speed flow cover a very large range, extending beyond the values typically found in the laboratory. Furthermore, the temperature gradients that are found in the boundary layer in supersonic flow lead to variations in Reynolds number across the layer in addition to the usual variation in the streamwise direction. To understand the effects of Reynolds number on turbulence in supersonic flow, we first need to consider the scaling of turbulence in subsonic flows.

8.2 Scaling Laws

The inner and outer-layer scaling scheme for the mean flow, as expressed by Equations 7.17 and 7.19, appears to be very successful in practice. A similar inner and outer scaling is therefore expected to apply to the time averaged turbulence statistics, and for the inner and outer regions of a subsonic boundary layer we expect, respectively:

$$\frac{\overline{u'^2}}{u_\tau^2} = f\left(\frac{yu_\tau}{\nu}\right), \tag{8.1}$$

and

$$\frac{\overline{u'^2}}{u_\tau^2} = g\left(\frac{y}{\delta}\right). \tag{8.2}$$

That is, we expect that the mean velocity and turbulence intensities scale with the same set of velocity and length scales: more precisely, that the velocity gradient and the turbulence intensities scale in this way. Matching the turbulence intensity in the overlap region leads to the conclusion that $\overline{u'^2}/u_\tau^2$ is constant in the log-law region. As we shall see, this is not observed in experiments. One explanation of this is that the "true" or *active* turbulent motion is overlaid by an irrotational *inactive* motion imposed by the pressure field of the large eddies in the outer part of the layer (Townsend 1956; Bradshaw, 1967, 1994). These eddies have length scales of order δ, and they are large compared to the scale of motions in the inner layer. However, as the wall is approached the v' component of the inactive motion must become small due to the wall constraint (the "splat" effect) so that its influence on the shear stress is minor, and the mean velocity log law is preserved.

Townsend (1976) proposed that

> ... the main eddies of the flow have diameters proportional to the distance of their centers from the wall, because the motion is directly influenced by its presence. In other words, the velocity fields of the main eddies, regarded as persistent, organized flow patterns, extend to the wall and, in a sense they are attached to the wall.

This is commonly known as Townsend's *attached eddy hypothesis*. He also proposed that the interaction between a large eddy and a smaller, viscous-dominated eddy occurs over several intermediate steps. Due to this highly indirect interaction, he proposed that the large-scale motion is essentially inviscid, and thus independent of the Reynolds number. This is known as Townsend's *Reynolds number similarity hypothesis*. Townsend did not regard the main eddies as having any particular shape, but to make his model quantitative, he assumed that the shear stress at a distance y from the wall was due principally to the eddies that have their center at that height. All the main eddies were assumed to be geometrically similar, and subject to the inviscid

boundary conditions at the wall where the normal component of velocity was assumed to be zero, but the other two components were allowed to have slip. If the probability density function of the eddy scales follows an inverse power law, then a constant stress region is obtained. Townsend's model therefore applies to the near-wall, fully turbulent part of the layer, and he found that

$$\frac{\overline{u'^2}}{u_\tau^2} = B_1 - A_1 \ln\left(\frac{y}{\delta}\right), \tag{8.3}$$

$$\frac{\overline{w'^2}}{u_\tau^2} = B_3 - A_3 \ln\left(\frac{y}{\delta}\right), \tag{8.4}$$

$$\frac{\overline{v'^2}}{u_\tau^2} = A_2. \tag{8.5}$$

Note that, by matching the gradients of the turbulence intensity in the inner and outer regions, rather than the intensity levels themselves, Equations 8.1 and 8.2 will also yield a logarithmic term in y/δ, without any recourse to the *pdf* of eddy scales. These relations indicate that the turbulence intensities are independent of the Reynolds number which is again at odds with the data, although Equations 8.3 to 8.5 may represent an infinite Reynolds number limit. The question remains as to what extent the turbulence profiles are similar in the sense that they collapse onto a Reynolds number independent curve, and what is the correct basis for the similarity argument.

8.2.1 Spectral Scaling for Incompressible Flow

It is useful to begin by considering the scaling of the turbulence spectra. For subsonic boundary layer flows, spectral scaling laws were first suggested by Townsend and later developed extensively by Perry and his co-workers. Based upon Townsend's attached eddy hypothesis and the flow visualization results of Head and Bandyopadhyay (1981) (see Section 8.4.2), Perry and Chong (1982) developed a physical model for near-wall turbulence. They assumed that a turbulent boundary layer outside the viscous region may be modeled as a forest of hairpin or Λ-shaped vortices, which originate at the wall and grow outward. Figure 8.1 shows three Λ-shaped vortices of different scales, and indicates their influence on the velocity field sensed by a probe at a position y. The probe will sense contributions to u' and w' from all eddies of scale y and larger. However, only eddies of scale y will contribute to v'. Therefore, u' and w' should follow similar scaling laws, whereas v' may follow a somewhat different scaling law. Using these ideas in conjunction with dimensional analysis, scaling laws can be derived for the energy spectra in the turbulent wall region, defined as $\nu/u_\tau \ll y \ll \delta$ (Perry et al., 1985, 1986). In general, it is the region where direct wall effects such as the damping of the velocity components are unimportant, and where the direct influence of the large-scale flow geometry

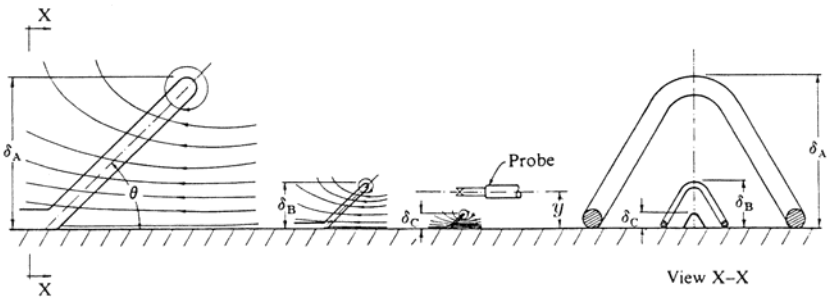

Figure 8.1. Sketch of the streamline patterns and spatial influence of attached eddies at three different scales. (Reproduced from Perry et al. (1986)). Copyright 1986, Cambridge University Press. Reprinted with permission.)

and outer boundary conditions can also be neglected. This region corresponds approximately to the overlap region in the mean velocity profile, that is, the region where the velocity has a logarithmic variation.

First consider the u-component of the turbulence fluctuations in an incompressible flow. Eddies of scale δ will contribute only to the large-scale, low wave number (low frequency) region of the energy spectrum Φ_{11}. For the large-scale eddies, viscosity is less important, and the spectrum in the low wave number region should depend only on u_τ, k_1, y, and δ, where k_1 is the streamwise component of the three-dimensional wave number vector $\mathbf{k}$. From dimensional analysis, the spectrum of u at low wave numbers should have the form

$$\frac{\Phi_{11}(k_1\delta)}{u_\tau^2} = g_1(k_1\delta) = \frac{\Phi_{11}(k_1)}{\delta u_\tau^2}. \tag{8.6}$$

Throughout this section, the argument of Φ_{ii} denotes the unit quantity over which the energy spectral density is measured, following Perry et al. (1986). Equation 8.6 represents an outer flow scaling because it describes the contribution of the large-scale eddies.

Eddies of scale y will contribute to the intermediate wave number range of the spectrum, whereas eddies of scale δ will not. In this range the spectrum should have the following inner flow scaling form,

$$\frac{\Phi_{11}(k_1 y)}{u_\tau^2} = g_2(k_1 y) = \frac{\Phi_{11}(k_1)}{y u_\tau^2}. \tag{8.7}$$

The smallest scale motions, which contribute to the high wave number range of the spectrum, depend on viscosity. Kolmogorov (1961) assumed that these small-scale motions are locally isotropic, and that their energy content depends only on the local rate of turbulence energy dissipation ϵ, and the

kinematic viscosity ν. Dimensional analysis leads to

$$\frac{\Phi_{11}(k_1\eta)}{\upsilon^2} = g_3(k_1\eta) = \frac{\Phi_{11}(k_1)}{\eta\upsilon^2}, \tag{8.8}$$

where η and υ are the Kolmogorov length and velocity scales respectively, defined by

$$\eta = \left(\frac{\nu^3}{\epsilon}\right)^{1/4} \qquad \text{and} \qquad \upsilon = (\nu\epsilon)^{1/4}. \tag{8.9}$$

In the high wave number region, therefore, the spectrum follows a Kolmogorov scaling.

Just as the mean flow exhibited an inner and outer scaling with a region of overlap, it is expected that Equations 8.6 and 8.7 will have a region of overlap (*Overlap Region I*), and that Equations 8.7 and 8.8 will have another region of overlap (*Overlap Region II*). These scalings are illustrated in Figure 8.2. It follows that in Region I the spectrum must have the form:

$$\frac{\Phi_{11}(k_1\delta)}{u_\tau^2} = \frac{A_1}{k_1\delta} = g_1(k_1\delta), \tag{8.10}$$

or

$$\frac{\Phi_{11}(k_1 y)}{u_\tau^2} = \frac{A_1}{k_1 y} = g_2(k_1 y), \tag{8.11}$$

where A_1 is a universal constant. That is, in the turbulent wall layer, the spectrum in Overlap Region I follows a k^{-1} scaling.

In Region II, it follows that

$$\frac{\Phi_{11}(k_1\eta)}{\upsilon^2} = \frac{K_o}{(k_1\eta)^{5/3}} = g_3(k_1\eta), \tag{8.12}$$

or

$$\frac{\Phi_{11}(k_1 y)}{u_\tau^2} = \frac{K_o}{\kappa^{2/3}(k_1 y)^{5/3}} = g_2(k_1 y). \tag{8.13}$$

Equation 8.12 was first derived by Kolmogorov (1961) using entirely different arguments. The region displaying a $k_1^{-5/3}$ scaling is called the *inertial subrange*, and K_o is called the Kolmogorov constant ($\approx$0.5). To derive these $k_1^{-5/3}$ scalings, Perry et al. (1986) imposed the requirement that the spectrum be independent of viscosity in the inertial subrange, and assumed that in the turbulent wall region dissipation equals production, $\varepsilon = -\overline{u'v'}\,(\partial u/\partial y)$, that the velocity profile is logarithmic, and that $-\overline{u'v'} = u_\tau^2$. Some spectra for the turbulent wall region are shown in Figure 8.3. The $k_1^{-5/3}$ and k_1^{-1} regions are evident. At high Reynolds numbers, a very long $k_1^{-5/3}$ range has been observed in the spectrum (Grant et al., 1962), but recent experiments in pipe flow have called into question presence of a k_1^{-1} similarity range at very high Reynolds numbers (Morrison et al., 2004).

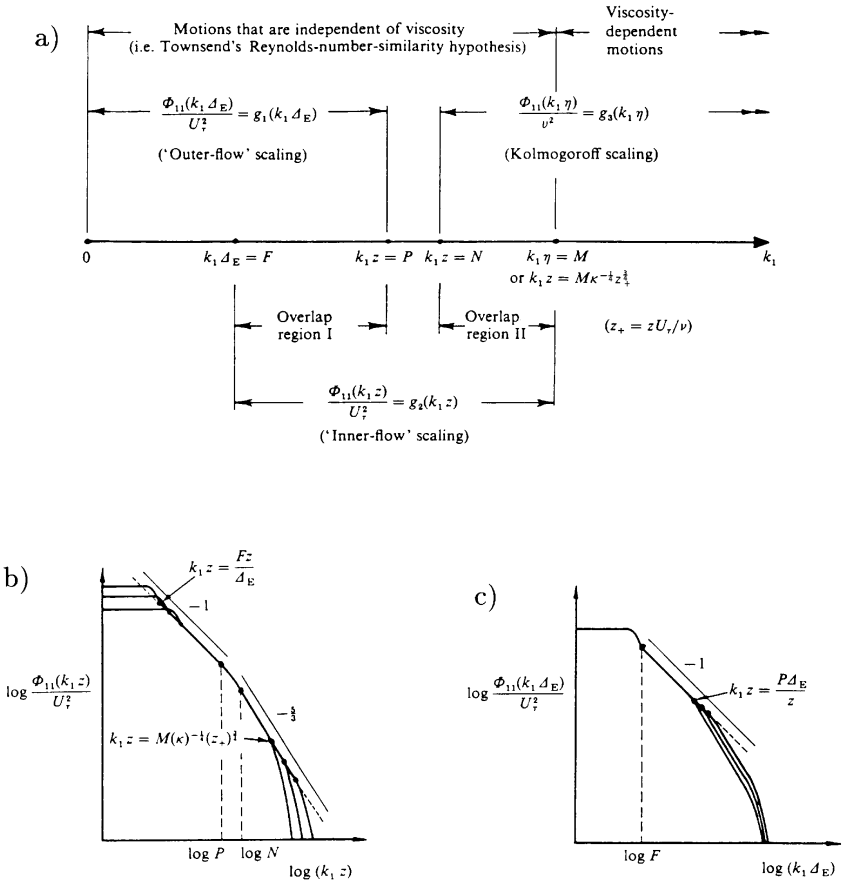

Figure 8.2. Behavior of the energy spectra of the longitudinal and spanwise velocity fluctuations, $\Phi_{11}(k_1)$ according to Perry et al. (see text). $\Phi_{33}(k_1)$ is expected to behave similarly. (a) Chart showing the different scaling regions, (b) inner scaling behavior, and (c) outer scaling behavior. Note that in Perry et al.'s notation, z is distance from the wall, and Δ_E is a boundary layer thickness, similar to δ. (Figure from Perry et al. (1986). Copyright 1986, Cambridge University Press. Reprinted with permission.)

According to these arguments, Φ_{33}, the spectra of w' will follow similar scaling laws, as illustrated in Figure 8.2a. The boundaries of the overlap regions are denoted by P, N, M, and F, where P, N, and M are universal constants, and F is a constant characteristic of the large scales, and likely to be Reynolds number dependent. Figures 8.2b and 8.2c illustrate the deduced

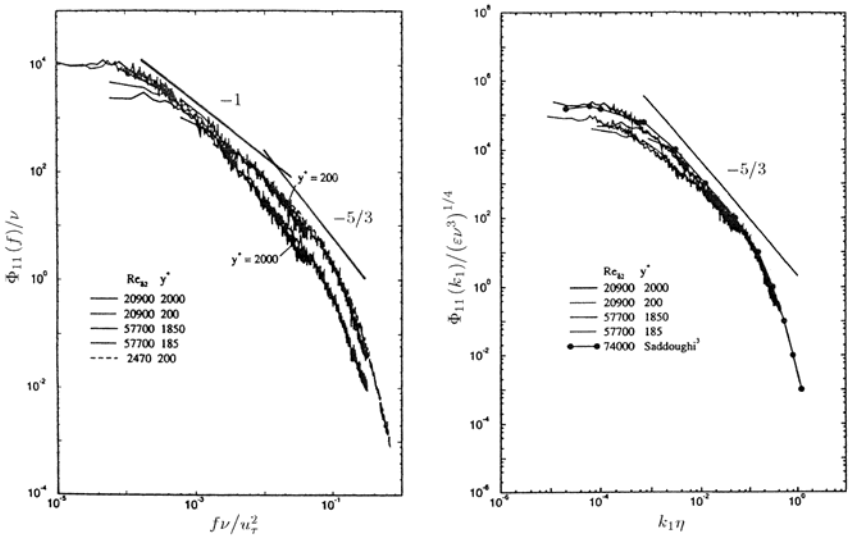

Figure 8.3. Spectra in the inner layer of subsonic boundary layers, plotted using inner layer scales (left), and Kolmogorov scales (right). (Adapted from Fernholz et al. (1995), with permission from Elsevier Science Ltd., Oxford, England.)

form of Φ_{11} and Φ_{33} using inner and outer scaling.

For the wall-normal component, Figure 8.1 suggests that there will be no contributions from δ-scale eddies, and thus there will be no outer flow scaling for Φ_{22}. There will only be inner flow and Kolmogorov scaling, with one region of overlap. Φ_{22} is described by Equations 8.7, 8.8, and 8.12, so that a region of $k_1^{-5/3}$ scaling is expected but not one in k_1^{-1}. Figure 8.4a summarizes the scaling laws for Φ_{22}, and Figures 8.4b and 8.4c illustrate the expected form of the v' spectrum using inner and outer scaling. Energy spectra measured by Perry and Abell (1975, 1977), Perry et al. (1985, 1986) Li (1989); Perry and Li (1990), Erm (1988); Erm et al. (1985), Smith (1994), and Zhao (2005) have all shown good agreement with these spectral scaling laws for the wall-normal component.

By integrating these spectral forms, Li (1989) and Perry and Li (1990) derived the following expressions for the normal stresses in a subsonic boundary layer:

$$\frac{\overline{u'^2}}{u_\tau^2} = B_1 - A_1 \ln\left(\frac{y}{\delta}\right) - V(y^+), \tag{8.14}$$

$$\frac{\overline{w'^2}}{u_\tau^2} = B_3 - A_3 \ln\left(\frac{y}{\delta}\right) - V(y^+), \tag{8.15}$$

$$\frac{\overline{v'^2}}{u_\tau^2} = A_2 - V(y^+), \tag{8.16}$$

where B_1 and B_2 are large-scale characteristic constants, particular to the flow geometry, and A_1, A_2, and A_3 are expected to be universal constants (all the constants are positive). The function $V(y^+)$ is a Reynolds number dependent, viscous correction term that increases with y^+, and it accounts for the dissipation region of the spectrum at finite Reynolds numbers. Equations 8.14 to 8.16 are valid only in the turbulent wall region.

Li (1989); Li and Perry (1989) and Perry et al. (1991) derived an expression for the total stress τ using an assumed form for the mean velocity profile (in this case Coles' combined law-of-the-wall/law-of-the-wake given by Equation 7.50). Figure 8.5 shows several Reynolds shear stress profiles calculated in this way, and the variation with Reynolds number is *not* monotonic because of low Reynolds number effects on the Coles wake factor.

Uddin (1994) and Marušić et al. (1997) extended these scaling laws to include the entire region outside the viscous sublayer. As with the mean flow, the deviation from the logarithmic profile near the wall is attributed to viscous effects, and the deviation in the outer part of the layer is due to wake effects. They suggested a "wall-wake" distribution where, for example,

$$\frac{\overline{u'^2}}{u_\tau^2} = B_1 - A_1 \ln\left(\frac{y}{\delta}\right) - V_{g1}(y^+) - W_{g1}\left(\frac{y}{\delta}\right). \tag{8.17}$$

They called V_{g1} the *viscous deviation*, and W_{g1} the *wake deviation*. Uddin gave empirical forms for V_{g1} and W_{g1} that agreed well with data over the range $6570 \leq Re_\theta \leq 35{,}100$ (V_{g1} was a more accurate version of the earlier function V). An extension of Equation 8.17 that applies across the entire boundary layer including the viscous near-wall layer was proposed by Marušić and Kunkel (2003), and comparisons with the laboratory data of DeGraaff and Eaton (2000) and the atmospheric data of Metzger et al. (2001) showed excellent agreement (Figure 8.6), although the formulation does not reproduce the outer peak in the streamwise intensity observed at high Reynolds numbers (as seen in Figure 8.11). A similar high level of agreement with high Reynolds number pipe flow data was shown by Marušić et al. (2004), despite the absence of a region of k_1^{-1} similarity in the streamwise velocity spectra (Morrison et al., 2004).

8.2.2 Spectral Scaling for Compressible Flow

These spectral arguments for the scaling of the turbulence can be extended to compressible flows, as follows (for further details see Dussauge and Smits (1995)). In the analysis of the mean velocity distributions in supersonic boundary layers it was assumed that the mixing length distribution was the same

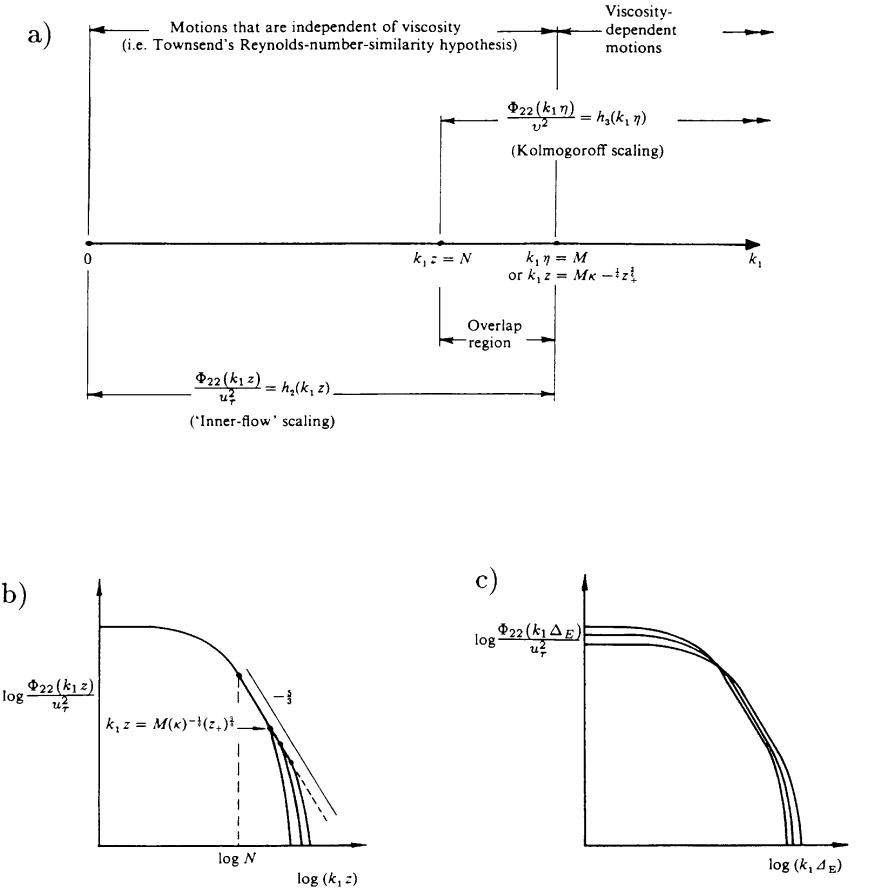

Figure 8.4. Behavior of the energy spectra of the wall-normal velocity fluctuations $\Phi_{22}(k_1)$, according to Perry et al. (see text). (a) Chart showing the different scaling regions, (b) inner scaling behavior, and (c) outer scaling behavior. Note that in Perry et al.'s notation, z is distance from the wall, and Δ_E is a boundary layer thickness, similar to δ. (Figure from Perry et al. (1986). Copyright 1986, Cambridge University Press. Reprinted with permission.)

as in subsonic flows. This comprises essentially a variable fluid property assumption; that is, the mechanisms governing turbulent transport are the same as at low speed, and the variations of density are taken in account by scaling the local stress (see Section 5.1). This hypothesis is quite successful, because, as we have seen, experimental evidence supports that the log law is observed in the transformed velocity profile with the same constants as found at low

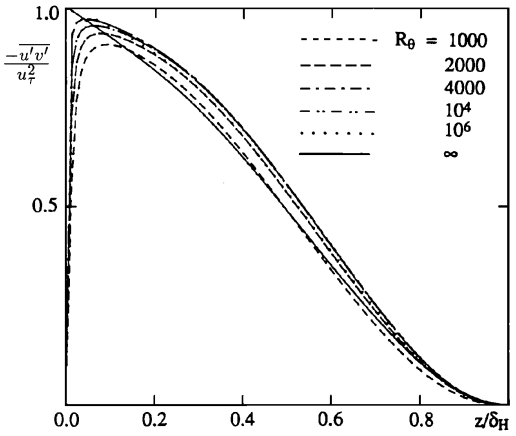

Figure 8.5. Theoretical Reynolds shear stress profiles, $-\overline{u'v'}/u_\tau^2$, derived by Li and Perry (1989), from which this figure is taken, with the authors' permission. In their notation, z is the distance from the wall, and δ_H $(=\Delta_E)$ is a boundary layer thickness similar to δ.

speeds. Therefore it may be expected that the typical size of the energetic eddies producing turbulent transport obeys the same laws as in subsonic flows. Note that this scale is built on the shear stress and that it is a scale related to turbulent diffusion.

Hence, the length scales for the low and intermediate wave number regions in the space $\nu/u_\tau \ll y \ll \delta$ are as in subsonic flow, that is, the boundary layer thickness δ (or equivalently, Δ), and the distance from the wall y, respectively. The velocity scale for both regions is $(\tau_w/\bar{\rho})^{1/2}$. By applying the overlap argument, we find that the k_1^{-1} power law is again obtained in Overlap Region I.

For compressible flow, however, the scaling of the viscous contribution to the spectrum will change because the Kolmogorov scales vary due to temperature gradients. We can define new length and velocity scales by considering the viscosity, the rate of dissipation per unit volume φ (not per unit mass ε), and the density. Dimensional analysis gives:

$$\eta' = \rho^{-1/2}\left(\frac{\mu^3}{\varphi}\right)^{1/4} \qquad \text{and} \qquad v' = \rho^{-1/2}\left(\mu\varphi\right)^{1/4}. \tag{8.18}$$

Equations 8.11 and 8.12 now have the form:

$$\frac{\Phi_{11}\left(k_1 y\right)}{\rho_w u_\tau^2/\rho} = g_2\left(k_1 y\right) = \frac{\Phi_{11}\left(k_1\right)}{y\rho_w u_\tau^2/\rho} \tag{8.19}$$

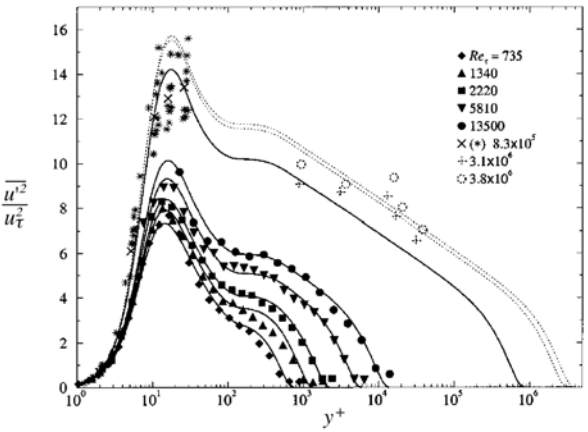

Figure 8.6. Comparison of Marušić and Kunkel (2003) formulation with data. Solid symbols are from DeGraaff and Eaton (2000), and symbols $*$ and $\times$ are from Metzger et al. (2001). Broken symbols are atmospheric surface data, which should be compared with the broken lines. (From Marušić and Kunkel (2003), with permission.)

$$\frac{\Phi_{11}\left(k_1\eta'\right)}{v'^2} = g_3\left(k_1\eta'\right) = \frac{\Phi_{11}\left(k_1\right)}{\eta' v'^2}. \tag{8.20}$$

So the Kolmogorov scales are unchanged as long as $\bar{\nu} \approx \bar{\mu}/\bar{\rho}$ and $\bar{\varepsilon} \approx \bar{\varphi}/\bar{\rho}$. The analysis for the overlap region is the same as for low-speed boundary layers: the Kolmogorov scales are determined in the equilibrium zone where production and dissipation are assumed to balance, where the turbulent shear stress is constant, and where the transformed velocity is logarithmic. It is again found that the spectrum of $\overline{u'^2}$ should have a range in $k_1^{-5/3}$. Because the analysis can be performed using either the incompressible or compressible variables, the changes in the scales due to variations in the mean density are absorbed in the modified dissipation rate because of the density scaling of the velocity gradient. The differences between the incompressible and the compressible definitions of the Kolmogorov scales depend mainly on the link between velocity and density in the part of the layer where dissipation is maximum, and therefore it should scale with the friction Mach number $M_\tau = u_\tau/a_w$.

It may then be inferred that for weak compressibility effects, the spectra for u' and w' have two wave number ranges with power-law variations in k_1^{-1} and in $k_1^{-5/3}$, as at low speeds. This analysis does not indicate where these wave number ranges are placed in the spectrum, that is, if high speeds produce larger or smaller energetic eddies, or induce a change in the orientation of these eddies. Naively, it also seems that the existence of a k_1^{-1} range should be

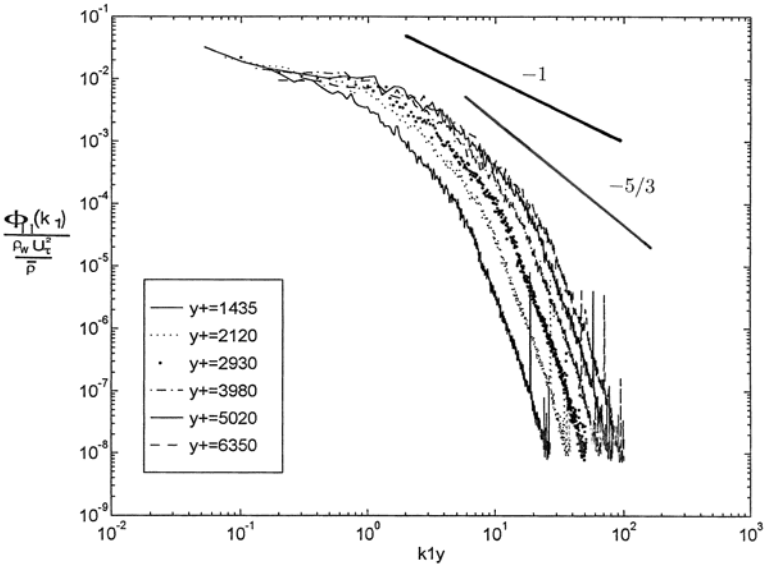

Figure 8.7. Spectra in a Mach 2.9 boundary layer at $Re_\theta = 78,000$. The data for $y^+ \leq 2930$ are in the logarithmic region. (Adapted from Spina (1988), with the author's permission.)

a rather robust feature, because the existence of two domains where the wave numbers scale respectively with δ and y are the only necessary conditions. The $k_1^{-5/3}$ law is expected to have less generality, because the existence of a constant shear stress zone with a logarithmic velocity distribution is postulated, and a balance between production and dissipation is also required. The data are somewhat ambiguous, as shown in Figure 8.7 for a Mach 2.9, high Reynolds number boundary layer: the $k_1^{-5/3}$ range is clearly evident, but the k_1^{-1} region seems to be rather small. These observations agree well with the high Reynolds number data of Morrison et al. (2004) in incompressible, fully developed turbulent pipe flow.

As a last remark, it may be seen that the incompressible and the compressible definitions of the Kolmogorov scales are equivalent for moderate Mach numbers, but in the buffer zone they may differ significantly from each other if the friction Mach number M_τ is close to 1. In this case, however, it may be expected that the hypotheses required for the derivation of the power laws will no longer be valid. In practice, friction Mach numbers are usually small (≤ 0.1), except at hypersonic Mach numbers and very high Reynolds numbers, or on extremely cold walls.

We see that the turbulence spectra give insight into the scaling of the turbulence stresses. There are some obvious shortcomings in the spectral arguments:

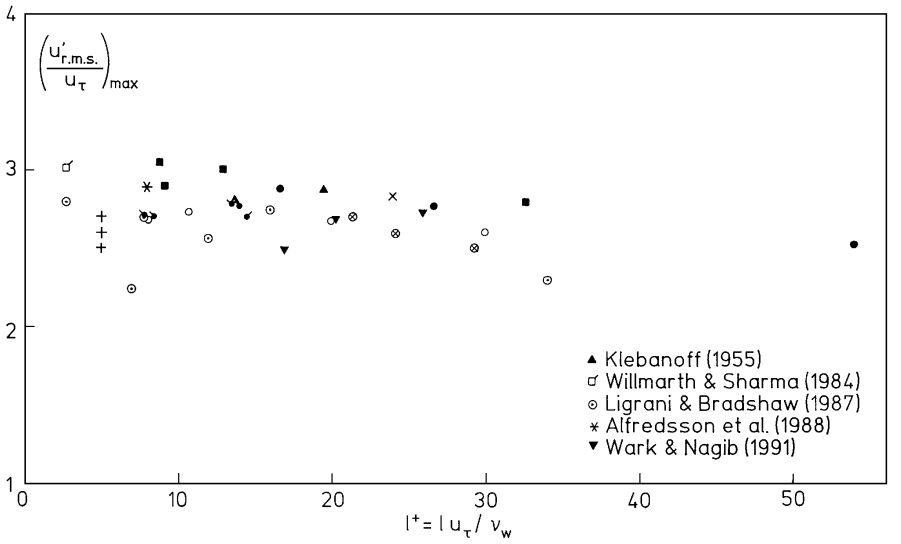

Figure 8.8. The influence of the characteristic dimensionless hot-wire length scale l^+ on the maximum value of $\sqrt{\overline{u'^2}}/u_\tau$ in subsonic boundary layers. $Re_\theta > 700$ and $l/\delta > 180$. (Figure from Fernholz and Finley (1996), where original references are given. Reprinted with permission from Elsevier Science Ltd., Oxford, England.)

in particular, the data are not uniformly supportive of the proposed scaling. Nevertheless, the physical arguments are reasonable, and they provide a starting point for understanding the likely effects of Reynolds and Mach number under conditions where Morkovin's hypothesis is satisfied.

8.3 Turbulence Data

In considering the stress behavior, it is useful to take the approach followed in the previous chapter where we used subsonic flows to try to identify Reynolds number trends, and then went on to examine supersonic flows in order to understand Mach number effects. The discussion given here draws heavily on the earlier reviews by Fernholz and Finley (1996) and Dussauge et al. (1996), although the presentation has been considerably extended. By way of a general comment, we need to be aware of the errors and uncertainties associated with the measurement techniques, particularly the systematic errors. For example, Figures 8.8 and 8.9 show how the finite length of the sensor affects the level of the maximum turbulence intensity measured in the near-wall region of subsonic boundary layers. As the wire length decreases, the level increases. Nevertheless, the data can be extrapolated reasonably unambiguously to zero sensor

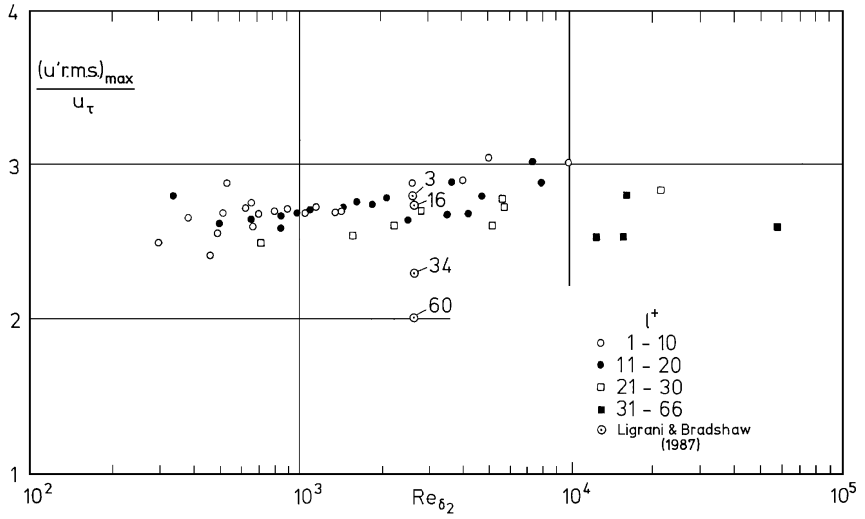

Figure 8.9. The influence of l^+ and Reynolds number on the maximum value of $\sqrt{\overline{u'^2}}/u_\tau$. (Figure from Fernholz and Finley (1996), where original references are given. Reprinted with permission from Elsevier Science Ltd., Oxford, England.)

length, and there is a definite trend where the level increases with Reynolds number, ranging from about 2.8 at $Re_\theta = 1000$ to about 3.2 at $Re_\theta = 10{,}000$. At still larger Reynolds numbers, this ratio can reach a value about 4 (see Figures 8.6 and 8.10). Note that in Figures 8.9 to 8.17, $Re_{\delta 2} = Re_\theta$, because all data shown are for subsonic flow. Marušić and Kunkel (2003) derived the variation of the maximum turbulence intensity with $Re_\tau = \delta u_\tau/\nu$ on the basis of their similarity formulation (Section 8.2.1) and found good agreement with the data. In later work, Marušić (2004) showed that the similarity formulation indicates that the maximum mean square value should follow the functional form:

$$\frac{\overline{u'^2}}{u_\tau^2} = a + b \ln Re_\tau, \tag{8.21}$$

and the agreement with experiment, including very high Reynolds number atmospheric data, is excellent (Figure 8.10).

8.3.1 Incompressible Flow

Figure 8.11 shows the distributions of $\overline{u'^2}$ normalized with wall variables. At all Reynolds numbers, similarity can be observed in the range $3 \leq y^+ \leq 50$, including the cases with high freestream turbulence levels, although the maximum value of $\overline{u'^2}/u_\tau^2$ tends to increase slightly with Reynolds number, as

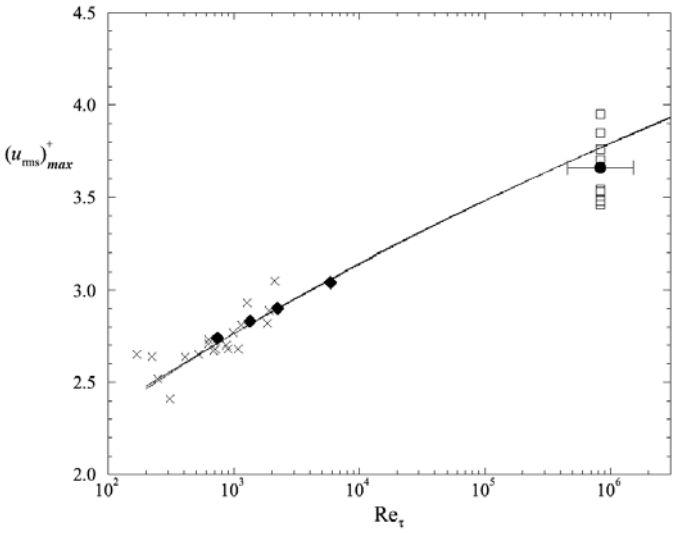

Figure 8.10. The maximum value of $\sqrt{\overline{u'^2}}\big/u_\tau$ in the near-wall region. The solid line is Equation 8.21 with $a = 0.9132$ and $b = 0.9737$. (From Marusic (2004), with permission.)

we noted above. The position where this maximum occurs, however, seems to be fixed at $y^+ \approx 15$ (Sreenivasan, 1988). For values of $y^+ > 100$ large departures are observed in inner scaling, with a tendency for the intensity to form a second maximum in a region corresponding to the mean-profile log law region, which becomes more pronounced as Re_θ increases. Such second peaks are often observed in high Reynolds number compressible boundary layers (Figures 3.1.1 and 3.1.2 in Fernholz and Finley (1981)), although generally not so pronounced.

The $\overline{u'^2}$ data plotted using the Rotta thickness as the outer length scale are shown in Figures 8.12 and 8.13. With this scaling the data collapse well for $y/\Delta > 0.4$ ($y/\delta > 0.1$) for $Re_\theta > 5000$ in the same way as the mean velocity profile (Figures 7.6 to 7.8). The second maximum shown in Figure 8.11 can be seen to represent a further extension of outer similarity toward the wall as Re_θ increases. Figure 8.12 shows the convergence of the $\overline{u'^2}$ profiles toward this universal behavior at lower Reynolds numbers.

At high enough Reynolds number, therefore, the $\overline{u'^2}$ profiles display similarity in the viscous sublayer and buffer layer when expressed in inner scaling, except for a continuing increase of the maximum turbulence intensity at $y^+ \approx 15$, which Morrison et al. (2004) ascribes to the influence of the inactive, outer layer motions on the near-wall turbulence. Morrison et al. suggest that

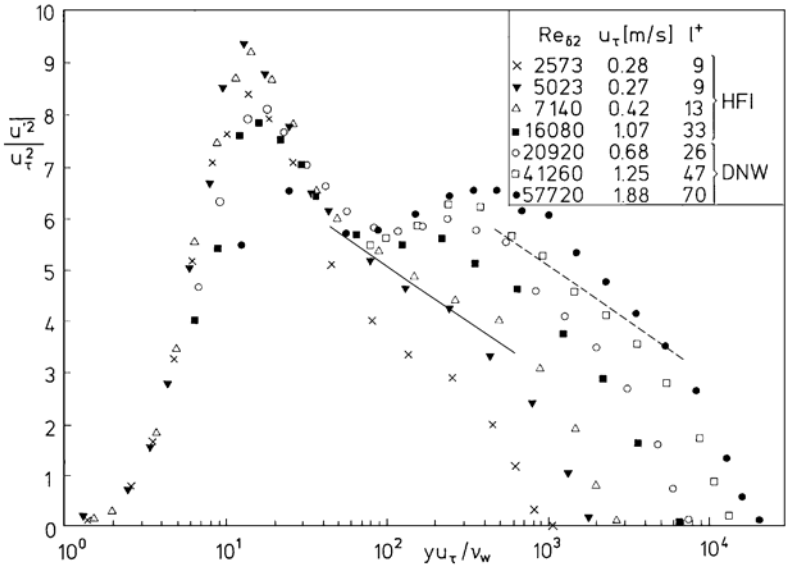

Figure 8.11. Distribution of the longitudinal Reynolds stress in inner layer scaling at medium to high Reynolds numbers. Data from Bruns et al. (1992) and Nockemann et al. (1994). ————, Equation 8.14 for $Re_{\delta 2} = 5023$; ---------, $Re_{\delta 2} = 57{,}720$. (Figure adapted from Fernholz and Finley (1996) with permission from Elsevier Science Ltd., Oxford, England.)

the interaction between inner and outer layer motions are responsible for such departures from strict Reynolds number similarity. In outer scaling, similarity is observed for $y/\delta > 0.4$, approximately. The formulation by Marušić and Kunkel (2003) shows very good agreement with the data at all Reynolds numbers in inner and outer regions, but the appearance of a second maximum in the streamwise component, seen in boundary layer and pipe data, is not reproduced.

The profiles of $\overline{v'^2}/u_\tau^2$ and $\overline{w'^2}/u_\tau^2$ plotted against y^+ (not shown here) display little or no sign of similarity. At least part of this behavior may be due to measurement errors. In particular, measurements of v' and w' using an X-wire probe are subject to errors due to spatial averaging caused by the separation L of the two wires. The dimensionless distance L^+ is likely to have as great an influence as l^+, and as a result v' and w' measurements are usually less precise than u' measurements (see Section 1.7.1).

Figures 8.14 and 8.15 show these data plotted against y/Δ. An orderly similarity behavior is found, although the peak values depend on Reynolds number again, this time quite markedly. The maximum value of $\overline{v'^2}/u_\tau^2$ in-

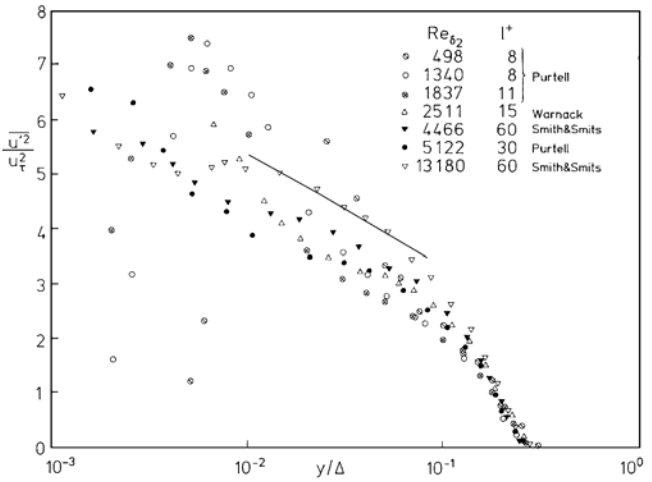

Figure 8.12. Distribution of the longitudinal Reynolds stress in outer layer scaling at low to medium Reynolds numbers. ————, Equation 8.14 for $Re_{\delta 2} = 5023$. (Figure adapted from Fernholz and Finley (1996) with permission from Elsevier Science Ltd., Oxford, England.)

creases from about 1 to 1.6 as Re_θ increases from about 600 to 60,000, and the maximum value of $\overline{w'^2}/u_\tau^2$ increases from about 2 to 3 over a similar Reynolds number range. The y^+ location of the peak for $\overline{v'^2}$ moves away from the wall as Re_θ increases, in agreement with the findings of Sreenivasan (1988). The location of the peak in $\overline{w'^2}$ cannot be determined with sufficient precision to make any meaningful conclusions.

For $\overline{v'^2}$ in the overlap region, comparisons with the predictions according to Equation 8.16 show a similar behavior to that found for $\overline{u'^2}$: good agreement is found with the data at the lower Reynolds numbers, but the increase with Reynolds number is underestimated somewhat. In a parallel study, Smith (1994) found a similar trend, and concluded that the additive constants in Equations 8.14 to 8.16 must be weakly Reynolds number dependent.

In contrast to the observations in boundary layers, recent data taken in a pipe flow indicate the presence of a region of constant v' in the overlap region where $\overline{w'^2}/u_\tau^2 \approx 1.3$, with a peak developing in the near-wall region ($y^+ < 100$ at higher Reynolds numbers (Zhao, 2005). Zhao interpreted this latter observation to demonstrate the increasing effect of the outer layer motions on the inner layer turbulence as the Reynolds number increases.

As far as the Reynolds shear stress is concerned, Sreenivasan (1988) and Sreenivasan and Sahay (1997) suggest "that the location of the peak Reynolds stress in a zero pressure gradient boundary layer is something like a critical

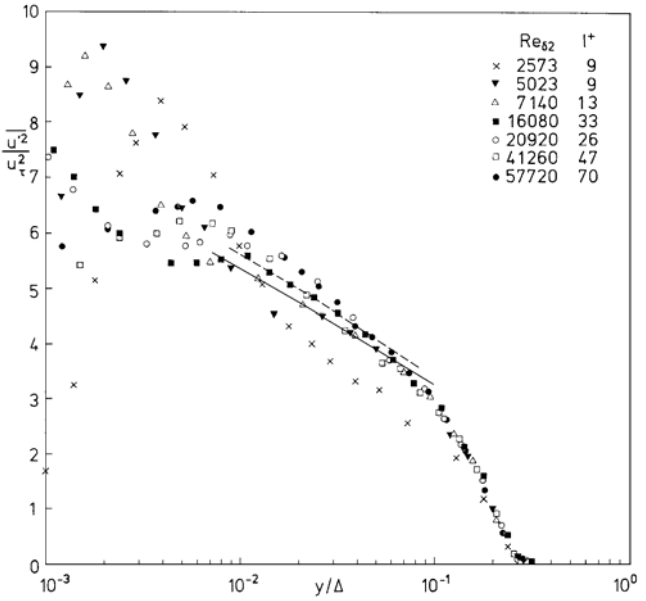

Figure 8.13. Distribution of the longitudinal Reynolds stress in outer layer scaling at medium to high Reynolds numbers. Data from Bruns et al. (1992) and Nockemann et al. (1994). ————Equation 8.14 for $Re_{\delta 2} = 5023$; --------- $Re_{\delta 2} = 57{,}720$. (Figure adapted from Fernholz and Finley (1996) with permission from Elsevier Science Ltd., Oxford, England.)

layer for the flow and that it shares some of the properties of the transitional critical layer." One of these properties is that the velocity of the mean flow in the transitional critical layer appears to be a constant fraction of the freestream velocity. For several wall-bounded shear flows Sreenivasan found $U_{crit} = 0.65U_e$, so that the position of this "critical" layer is in the logarithmic region of the boundary layer.

Similar ideas have been recently proposed by Wei et al. (2005) who derived a new scaling scheme for wall-bounded flows using the streamwise momentum equation and developing arguments based on stress gradients. For the mean flow, they identify two layers that lie between the traditional linear sublayer and the outer wake region: a stress gradient balance layer extending from the viscous-dominated flow near the wall well into the region where the log law is normally assumed to begin, and a viscous-advection balance or "meso-layer" occurring in the region where the maximum Reynolds shear stress is found, corresponding to Sreenivasan's critical layer. The extent of both layers increases with Reynolds number according to $\Delta y^+ \sim \sqrt{\delta^+}$, but of the two layers the stress gradient balance layer is of most interest because its velocity

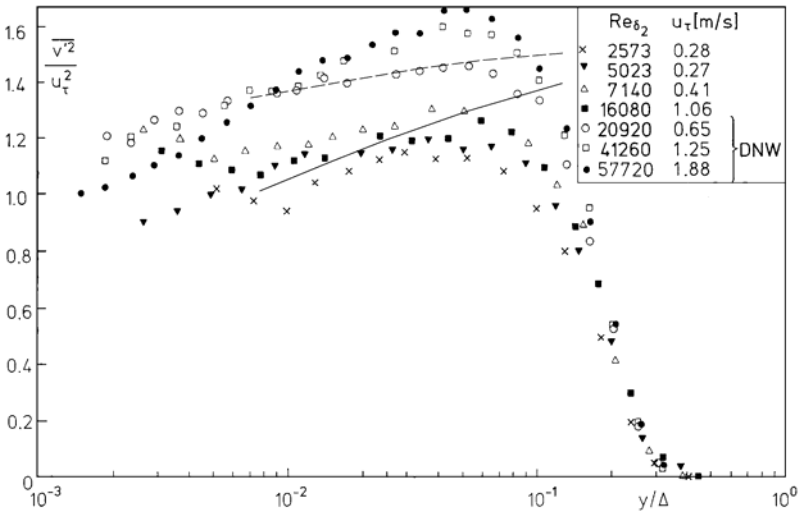

Figure 8.14. Distribution of the wall-normal Reynolds stress in outer layer scaling at medium to high Reynolds numbers. ———— Equation 8.16 for $Re_{\delta 2} = 5023$; - - - - - - - - $Re_{\delta 2} = 57{,}720$. (Figure adapted from Fernholz and Finley (1996), where original references are given, with permission from Elsevier Science Ltd., Oxford, England.)

increment is nearly constant and equal to about $U_e/2$, and it can occupy a substantial fraction of the layer (from $y^+ \approx 3$ to $y^+ \approx 1.6\sqrt{\delta^+}$. These observations may help to explain the power-law variation seen in the near-wall region by Zagarola and Smits (1998a), which blends into a logarithmic variation only for $y^+ > 600$, because it would appear that this power-law region and the stress gradient balance layer occupy similar space.

The scaled shear stress $-\overline{u'v'}/u_\tau^2$ in inner-layer scaling shows a plateau in the vicinity of its peak value of about 0.92 and 0.95 (for details see Fernholz and Finley, 1996). The spatial resolution of X-wire probes near the wall is generally poor, and the near-wall observations are not precise enough to confirm Spalart's (1988) suggestion that the total shear stress approaches the wall with a finite nondimensional slope of order -0.6, with the slope falling to zero only in the buffer layer.

Figure 8.16 shows the shear stress data in outer layer scaling. The data collapse for $y/\Delta > 0.09$. The peak value of the shear stress shows almost no dependence on Reynolds number, but in this scaling the location of the peak moves towards the wall as the Reynolds number increases. When expressed in terms of inner scaling, the peak moves away from the wall with increasing Reynolds number, although the movement of the peak is less pronounced

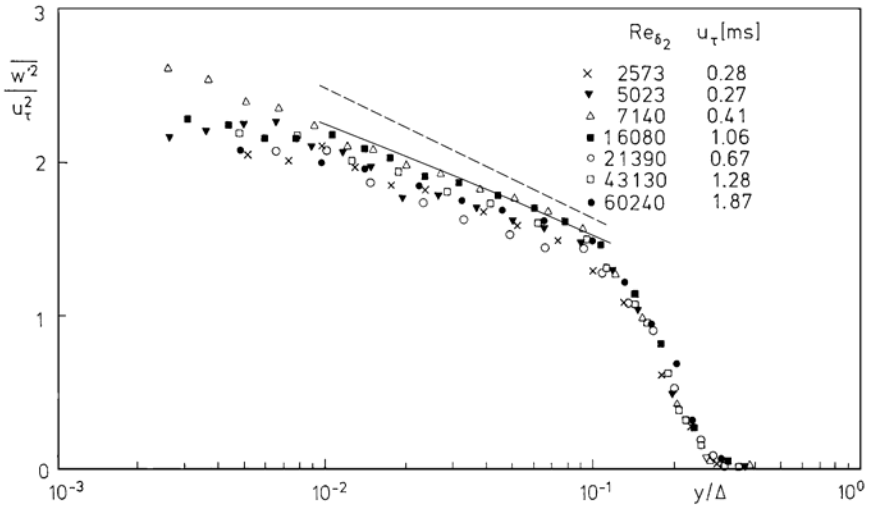

Figure 8.15. Distribution of the spanwise Reynolds stress in outer layer scaling at medium to high Reynolds numbers. Data from Bruns et al. (1992) and Nockemann et al. (1994). ———— Equation 8.15 for $Re_{\delta 2} = 5023$; - - - - - - - - - $Re_{\delta 2} = 57{,}720$. (Figure adapted from Fernholz and Finley (1996), with permission from Elsevier Science Ltd., Oxford, England.)

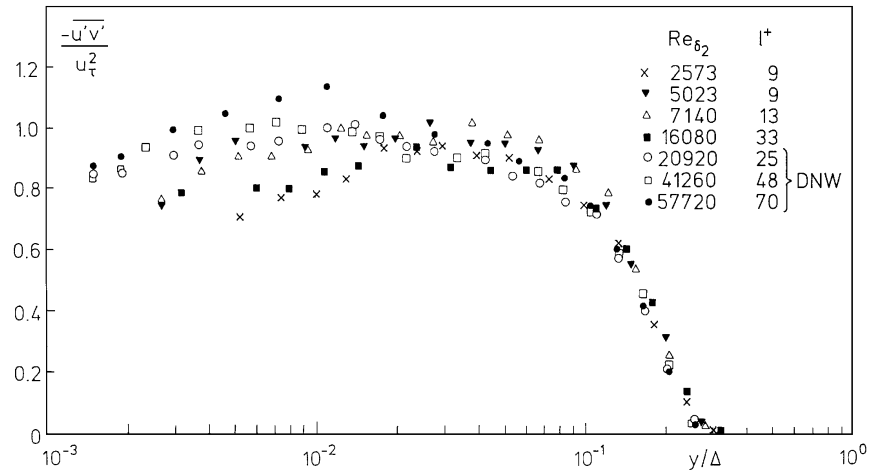

Figure 8.16. Distribution of the Reynolds shear stress in outer layer scaling at medium to high Reynolds numbers. Data from Bruns et al. (1992) and Nockemann et al. (1994). (Figure from Fernholz and Finley (1996). Reprinted with permission from Elsevier Science Ltd., Oxford, England.)

than for $\overline{v'^2}$. This is in qualitative agreement with the results collected by Sreenivasan (1988), who noted that the part of the dynamics contributing to the Reynolds shear stress does not reside either at constant y^+ or at constant y/Δ, again hinting at the influence of outer scales on the inner layer behavior.

Direct numerical simulations give shear stress values near the wall which are generally in good agreement with the experimental values obtained at the same Reynolds number. For example, at $Re_\theta = 670$, Spalart (1988) finds a maximum value of $\overline{u'v'}/u_\tau^2$ of about 0.95 (compared with the experimental value of 0.87 found by Erm and Joubert (1991)), and Yeung et al. (1993) find a maximum value of about 0.89. The position of the maximum value also agrees well with experiment (for further details see Fernholz and Finley (1996)). In other respects, as in the turbulent stress and skewness and flatness distributions, the DNS results agree similarly well with the experimental data (Erm et al., 1994).

Some particular ratios of stresses are also of interest. The "structure parameter" a_1 is the ratio of the Reynolds shear stress to the turbulent kinetic energy, and Klebanoff (1955) found it to be approximately constant in a range $0.1 \leq y/\delta \leq 0.8$, at a Reynolds number $Re_\theta = 7660$. Erm (1988) found similar results in the range $697 \leq Re_\theta \leq 2788$, with a_1 taking values between 0.14 and 0.16. Higher Reynolds number data are shown in Figure 8.17 in outer scaling. The location of the peak value is approximately constant, and the magnitude of the peak value lies between 0.14 and 0.17, increasing slightly with Re_θ.

The correlation coefficient R_{uv} increases from about 0.3 near the wall to about 0.45 in the outer part of the layer (see, for example, Klebanoff's (1955) results in Figure 8.21), and there is a weak tendency for these values to decrease with Reynolds number. The anisotropy ratio $\sqrt{\overline{v'^2}}/\sqrt{\overline{u'^2}}$ increases across the boundary layer from a value of about 0.4 to about 0.8, and shows the same strong Reynolds number dependence as $\overline{v'^2}$ itself (see also Smith (1994)). The ratio $\sqrt{\overline{w'^2}}/\sqrt{\overline{u'^2}}$ is nearly constant at a value of between 0.6 and 0.7 at all y-locations and Reynolds numbers.

As for the higher-order moments, the skewness and flatness of u' (given by $\overline{u'^3}/{u'_{rms}}^3$ and $\overline{u'^4}/{u'_{ms}}^2$, respectively) appear to be independent of Reynolds number when scaled using the appropriate scaling parameters for each region, as found by Smith (1994) and Fernholz and Finley (1996). The behavior of the triple correlations and production terms is discussed by Murlis et al. (1982), Erm (1988), Fernholz and Finley (1996), and Morrison et al. (1992).

8.3.2 Compressible Flow

In Chapter 1 we saw that when the longitudinal velocity fluctuations are normalized by the shear velocity $\overline{u'^2}/u_\tau^2$, there is a decrease in fluctuation level with increasing Mach number (see Figure 1.5). However, when the streamwise normal stress $\bar{\rho}\overline{u'^2}$ is normalized by the wall shear stress, the results are in fair

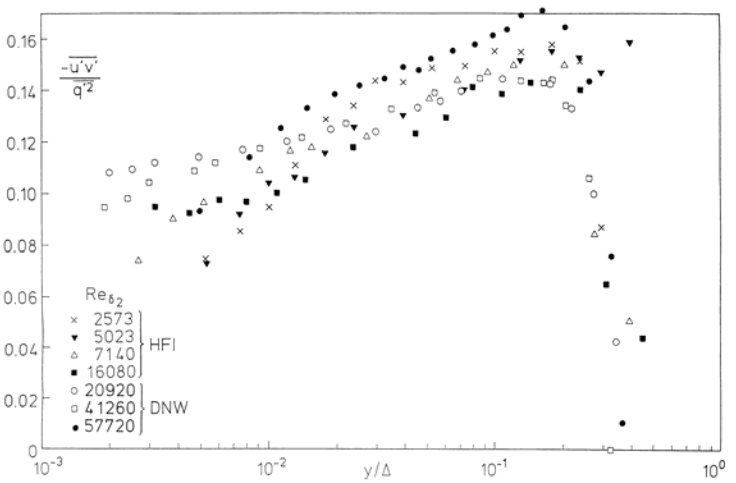

Figure 8.17. Distribution of the structure parameter $a_1 = -\overline{u'v'}/q^2$ in outer layer scaling at medium to high Reynolds numbers. Data from Bruns et al. (1992) and Nockemann et al. (1994). (Figure from Fernholz and Finley (1996). Reprinted with permission from Elsevier Science Ltd., Oxford, England.)

agreement with the incompressible data of Klebanoff (1955), except near the wall where the supersonic measurements are subject to considerable uncertainty (see Figure 1.2). This indicates the success of the scaling suggested by Morkovin (1962) to account for the mean density variation, and provides some support for the discussion given in Section 8.2. It should be mentioned that Fernholz and Finley (1981), in considering an earlier set of data, concluded that the streamwise Reynolds stress did not show a similar behavior in the outer region, no matter which velocity scale was used in the nondimensionalization. It appears that the later data shown in Figure 1.2 display a more regular behavior. Morkovin's scaling appears to be appropriate to at least Mach 5. Measurements by Owen et al. (1975) at $M_e = 6.7$ and Laderman and Demetriades (1974) at $M_e = 9.4$ exhibit damped turbulent fluctuations, particularly near the wall. Because both of the hypersonic data sets are for cold-wall conditions, this may simply indicate the stabilizing effect of cooling.

Measurements of $\overline{v'^2}$ and $\overline{w'^2}$ are less common than those of $\overline{u'^2}$, the data exhibit more scatter, and the conclusions are therefore less certain. Crosswire measurements of both streamwise and wall-normal components of velocity have suggested that some aspects of boundary layer structure depend on Mach number (Smits et al., 1989). In contrast to the streamwise turbulence intensity, $\overline{v'^2}$ and $\overline{w'^2}$ appear to increase slightly with increasing Mach number (Fernholz and Finley, 1981). In this case, Morkovin's scaling does not collapse the data,

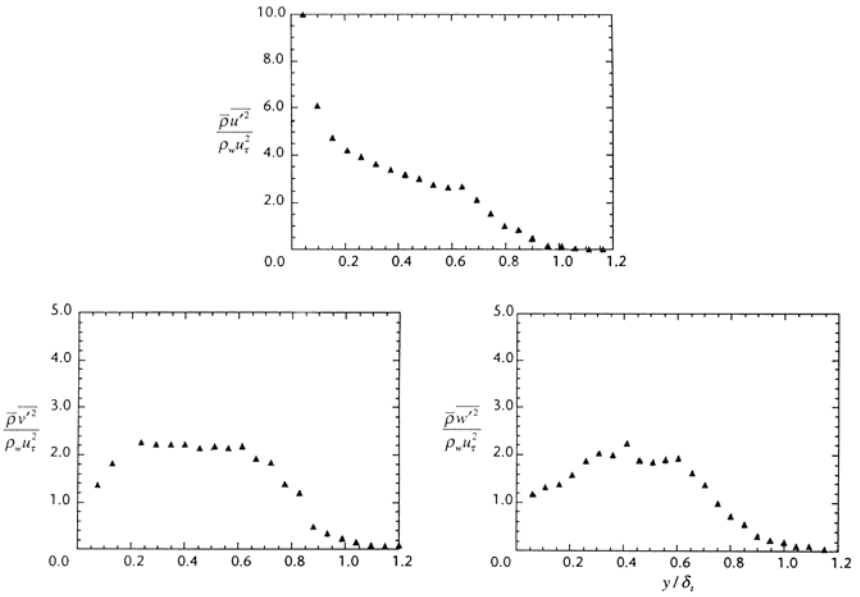

Figure 8.18. Turbulence distributions in a Mach 2.9 boundary layer, measured using hot-wire probes (Re_θ = 65,000). (Adapted from Konrad (1993), with the author's permission.)

and $\overline{\rho v'^2}/\tau_w$ and $\overline{\rho w'^2}/\tau_w$ show no obvious trend toward similarity. Using hot-wire anemometry, Konrad (1993) found that $\overline{w'^2}$ and $\overline{v'^2}$ in a Mach 2.9, high Reynolds number boundary layer were approximately equal throughout the layer (see Figure 8.18). In contrast, the measurements by Eléna and Lacharme (1988) in a Mach 2.3, low Reynolds number boundary layer using laser-Doppler velocimetry indicate that the behavior of $\overline{v'^2}/{u_\tau}^2$ is almost identical to that found in subsonic flows (see Figure 8.19). The behavior of the anisotropy ratio is therefore not clear: Eléna and Lacharme data indicate that the ratio $\overline{v'^2}/\overline{u'^2}$ is almost the same as those found by Klebanoff (1955) in a subsonic boundary layer, whereas the measurements by Fernando and Smits (1990) and Konrad (1993) indicate that this ratio increases with Mach number. As we saw earlier, however, the anisotropy depends strongly on Reynolds number, primarily because of the behavior of $\overline{v'^2}$, and the differences between the two sets of compressible flow data may well be due to the large Reynolds number difference between the experiments. Although the evidence is not conclusive, there may be no significant Mach number influence.

Recent DNS results on a zero pressure gradient boundary layer by Martin (2003, 2004) cover a Mach number range from 3 to 8, where the value of δ^+ was held approximately constant at 400 (corresponding to $Re_\theta = 2390$ at the lowest

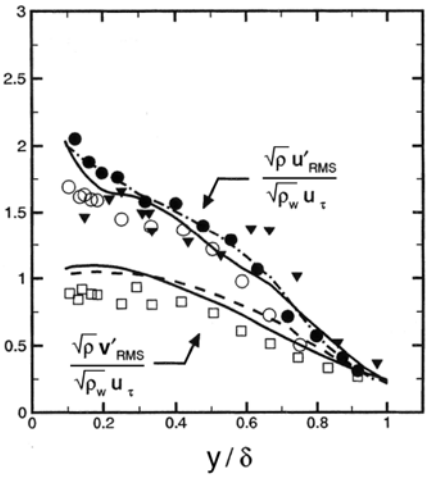

Figure 8.19. Turbulence distributions in a Mach 2.3 boundary layer ($Re_\theta = 4000$ to 4700). Symbols: Experimental results obtained using LDV (Eléna and Lacharme, 1988). Solid lines: DNS; broken lines: subsonic data from Klebanoff (1955). (Figure adapted from Martin (2004), with permission of the author.)

Mach number, and $Re_\theta = 13,060$ at the highest Mach). The wall condition was chosen to be isothermal with a value close to the adiabatic value, and the effect of varying the wall temperature was examined at Mach 5. As reported by Smits and Martin (2004), the DNS results support many of the experimental observations. For example, the mean velocity profiles transformed according to van Driest collapse with the usual scaling using inner and outer variables, and the Reynolds stresses collapse using Morkovin's scaling at about the same level of accuracy as seen in experiment. One of the cases considered by Martin was at $M = 2.23$ and $Re_\theta = 4452$, corresponding to the experiments by Debiève (1983), Eléna et al. (1985), and Eléna and Lacharme (1988), where $Re_\theta = 4000$ to 4700. The comparisons between DNS and experiment are particularly impressive (Figure 8.19).

Sandborn (1974) reviewed direct measurements and indirect evaluations of the Reynolds shear stress $-\overline{\rho}\overline{u'v'}$ in zero pressure gradient flows (a later, more comprehensive study was provided by Fernholz and Finley (1981)). Sandborn constructed a "best fit" of normalized shear stress profiles (τ/τ_w) from integrated mean-flow data taken over a wide Mach number range ($2.5 < M_\infty < 7.2$: extended to Mach 10 for adiabatic and cold walls by Watson (1978)). The data indicate a near-universal shear stress profile that agrees well with the incompressible measurements of Klebanoff (1955) (see Figure 8.20). Direct measurements of the shear stress have exhibited only modest agreement with

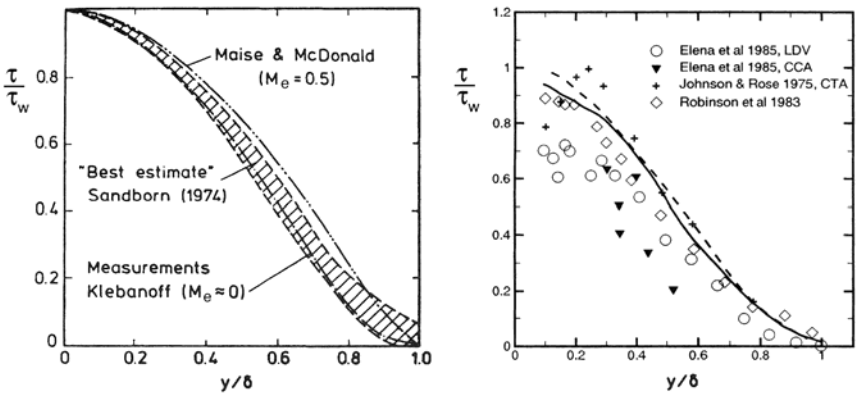

Figure 8.20. Distribution of shear stress in boundary layers at supersonic speed. Left: Figure from Sandborn (1974). Right: Figure from Martin (2004), where the solid line is DNS, and the broken line is subsonic data from Klebanoff (1955). (Figures reprinted with permission of the authors.)

Sandborn's best fit. The agreement is limited to the outer layer, with great scatter in the inner layer and most profiles not tending toward $\tau/\tau_w = 1$ near the wall. The data in the inner layer do not scale with yu_τ/ν_w, almost certainly because of the difficulties with the measurements. In contrast, the DNS results of Martin (2004) shown in Figure 8.20 are in excellent agreement with Sandborn's curve, and the Mach 2.32 LDV data of Eléna et al. (1985).

The shear correlation coefficients obtained by Fernando and Smits (1990) at Mach 2.9, indicated that R_{uv} decreases significantly with distance from the wall, from a value of about 0.45 near the wall to about 0.2 near the boundary layer edge (see Figure 8.21). This is in contrast to most subsonic flows where the correlation coefficient is nearly constant at a value of about 0.45 in the region between 0.1δ and 0.8δ. As can be seen in the figure, the data by Eléna and Lacharme (1988) at Mach 2.3 follow the subsonic distribution closely, and it is difficult to say how compressibility affects the level of R_{uv} without further experiments. However, as noted earlier, there is about a factor of 15 difference in Reynolds number between the results of Fernando and Smits and Eléna and Lacharme, and the differences seen in the distribution of R_{uv} may well reflect that fact, primarily through the Reynolds number dependence of $\overline{v'^2}$ (see Figure 8.14).

In Section 5.2 the Strong Reynolds Analogy was discussed, and some measurements in support of this analoguey were presented in Figures 5.4 and 5.5. It appears that the SRA is closely followed in supersonic boundary layers on adiabatic walls, and that the correlation coefficient R_{uT} is approximately equal to -0.8 throughout the layer. The DNS results of Wu and Martin (2004) at

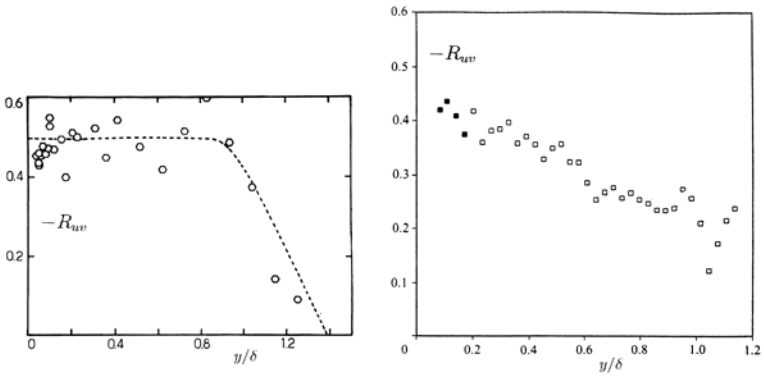

Figure 8.21. Distribution of R_{uv} in subsonic and supersonic boundary layer. Left: Data from Eléna and Lacharme (1988) (the dotted line is the subsonic data of Klebanoff (1955)). (Reprinted with permission of Gauthier-Villars.) Right: Data from Fernando and Smits (1990) (the filled-in symbols are subject to errors due to transonic effects). (Copyright 1990, Cambridge University Press. Reprinted with permission.)

Mach 3 agree very well with these observations (Figure 8.22), as do the computations by Martin (2004) for Mach numbers from 3 to 8. The magnitude of R_{uT} is considerably higher than that found in slightly heated subsonic flows, as seen in Figure 5.5, and the reason is not entirely clear. However, the high level of the correlation makes the SRA a very useful tool in describing the behavior of supersonic turbulent boundary layers, especially in formulating turbulence models. The SRA can also be extended to nonadiabatic flows, as discussed in Chapter 9.

The stagnation temperature fluctuation must be known to evaluate the turbulent heat-flux correlation, $-c_p\overline{\rho}\overline{v'T'}$. Kistler (1959) observed that $T'_{0_{rms}}/\overline{T_0}$ increased with Mach number, with maxima of 0.02 at $M_\infty = 1.72$ and 0.048 at $M_\infty = 4.67$. If Kistler's data are nondimensionalized using T_w (Fernholz and Finley, 1981) or $T_r - T_e$ (Sandborn, 1974), the Mach number dependence appears to be eliminated, but similarity of the stagnation temperature distributions is not achieved. The same conclusions are reached from measurements by Morkovin and Phinney (1958) and Horstman and Owen (1972). The maximum level of stagnation-temperature fluctuations is about 6% (for $M < 7$). Further analysis of these data shows that $T'_{0_{rms}}$ scales according to either $T_{0e} - T_w$ or $T_{0e} - T_r$. The fluctuations in total temperature appear to be produced by the difference in stagnation temperature between the wall and the freestream, and not, for example, by the unsteadiness in pressure through the term $\partial p/\partial t$ in the total enthalpy equation. In these experiments, the maximum of $T_{0_{rms}}/(T_{0e} - T_r)$ is about 0.5, regardless of the Mach number, a rather

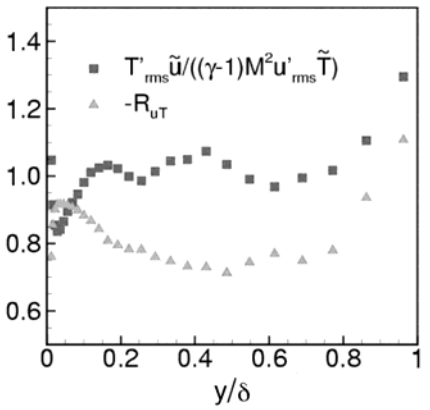

Figure 8.22. DNS results for the SRA in a Mach 3 boundary layer ($Re_\theta = 2400$). (Figure adapted from Wu and Martin (2004), with the authors' permission.)

satisfactory result because it shows that the total temperature fluctuations are of the order of (but less than) the total temperature difference across the boundary layer. Finally, T'_{0rms}/T_o is less than u'_{rms}/U and T'_{rms}/T, but not low enough to satisfy the strict Strong Reynolds Analogy. In fact, as indicated in Section 5.3, the one-dimensional form of the energy equation, together with the empirical results on the SRA, indicate that the ratio $T'_{0_{rms}}/T'_{rms}$ is approximately equal to $\sqrt{2\,(1+R_{uT})}$; that is, $T'_{0_{rms}}$ is about 60% of T'_{rms}, independent of the Mach number (Smits and Dussauge, 1989).

8.4 Organized Motions

Here we describe the organized, spatially correlated motions found in turbulent boundary layers. The interest in such flow structure is driven, at least in part, by the hope that a better understanding of the dynamics of turbulent motions will lead to a better predictive capability. Although we have not yet achieved that objective completely, our studies of organized motions have led to a deep (albeit largely qualitative) understanding of the turbulence production cycle in wall-bounded flows, and a much better understanding of Reynolds number scaling. The presentation given here is based largely on the earlier work by Smith (1994), Spina et al. (1994), Dussauge et al. (1996) and Smits and Delo (2001), and further details are given there. There are several excellent reviews of turbulent flow structure in the literature, including Willmarth (1975); Cantwell (1981), Robinson (1991a), and especially the volume by Panton (1997). More personal interpretations are offered by Hussain (1983), Coles (1987), and Sreenivasan (1989).

The term "structure" has at least two different interpretations. First, it is used to describe the behavior of the mean flow and Reynolds stresses. The scaling of the mean flow and Reynolds stresses, the composition of Reynolds stresses, anisotropy ratios, and the behavior of the shear correlation coefficient, Townsend's structure parameter a_1, and the intermittency profiles, can all be viewed as describing the structure of a turbulent boundary layer. Second, the term is used to describe coherent organized motions occurring in the flow. Robinson (1991a) defines a coherent motion, or structure, as

> a three-dimensional region of the flow over which at least one fundamental flow variable (velocity component, density, temperature, etc.) exhibits significant correlation with itself or with another flow variable over a range of space and/or time that is significantly larger than the smallest local scales of the flow.

This definition is quite general, although as Kline and Robinson (1989) point out, the classification of coherent structures in turbulent boundary layers can be arranged in many ways, and they use the term "quasi-coherent" to emphasize that the structures or motions exhibit significant variation from one experiment to another. More specific versions have been proposed (for instance, Hussain (1983)), but in essence they are just restricted forms of Robinson's definition.

8.4.1 Inner Layer Structure

Klebanoff (1955) found that about 75% of the total turbulence production in the boundary layer occurs in the region where $y/\delta < 0.2$. Most subsequent investigations of turbulent boundary layer structure have therefore focused on the near-wall region, primarily the viscous sublayer and buffer layer. Because of practical considerations, such as the need for adequate resolution of small scales, these studies have been limited to subsonic flows, predominantly at low Reynolds numbers; that is, $Re_\theta < 5000$. In supersonic flows, the scaling of the turbulence in the inner layer undoubtedly becomes more complicated because strong gradients of temperature occur in the near-wall region that can cause major changes in density and viscosity. Almost no near-wall data exist for supersonic boundary layers, and so we must proceed under the assumption that similar mechanisms occur in compressible flows, as long as Morkovin's hypothesis is satisfied. Recent DNS computations help verify this assumption, as discussed below.

Runstadler et al. (1963), Kline et al. (1967), and Bakewell and Lumley (1967) discovered that the viscous sublayer is occupied by alternating streaks of high- and low-speed fluid (relative to the mean), as illustrated in Figure 8.23. The spanwise spacing of the streaks λ_s was found to scale on inner variables and to have a nondimensional mean value of $\lambda_s^+ \approx 100$. The streaks were presumed

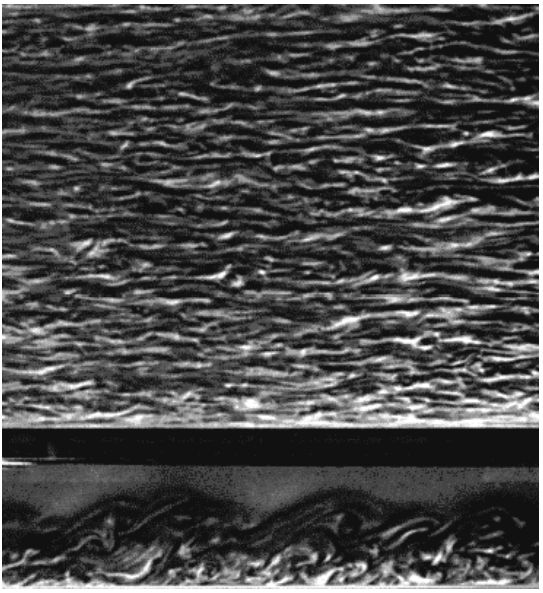

Figure 8.23. Turbulent boundary layer on a flat plate. The water was seeded with aluminum particles and viewed simultaneously from above and the side. Note the large population of meandering near-wall streaks in the top view, and the downstream-leaning, large-scale structure in the side view (Cantwell et al., 1978). (Copyright 1978, Cambridge University Press. Reprinted with permission.)

to be the result of elongated, counter-rotating streamwise vortices very near the wall. Kline et al. observed that the low-speed streaks would gradually lift up from the wall, oscillate, and then break up violently, ejecting fluid away from the wall and into the outer layer. They coined the term *bursting* to describe this sequence of events, and concluded that all the events comprising the bursting process were consistent with a stretched and lifted vortex. Kim et al. (1971) determined that in the wall region $0 < y^+ < 100$, nearly all of the turbulence production occurs during bursting, thus establishing the dynamical significance of the near-wall region and the bursting process.

Similar observations were made by Corino and Brodkey (1969). They found a recurring sequence of events where a large-scale disturbance would frequently impinge upon a near-wall region of low-speed fluid. This would be followed by one or more ejections of low-speed fluid up into the large-scale disturbance, resulting in violent chaotic interaction. Once the ejection(s) had subsided, a large region of high-speed fluid would cleanse the area of the debris of the interaction. Corino and Brodkey called this latter event a *sweep*. As the Reynolds number increased, the frequency and intensity of the ejection events

increased, and at high Reynolds numbers it was difficult to distinguish between individual events.

Cantwell (1981) examined the coherent structures in the inner layer in terms of localized regions of vorticity, and suggested that a fluctuating array of streamwise counterrotating vortices densely covers all parts of the smooth wall. Slightly above the streamwise vortices but still quite close to the wall is a layer that is regularly battered by bursts that involve very intense small-scale motions of energetic fluid, which he termed "energetic near-wall eddies."

The average spanwise spacing of the streaks ($\lambda_s^+ \approx 100$) is one of the few universally accepted aspects of boundary layer structure, although there are large departures from the mean (Smith and Metzler, 1983). In contrast, estimates of the streamwise extent of the streaks vary widely. This is most likely due to the different methods used to make the estimates. The low-speed streaks are seen to extend up to $L_x^+ = Ł_x u_\tau/\nu \approx 2000$ in some cases, when the spanwise meandering of the streaks is taken into account. Marušić (2004) has observed even longer streaks in moderate Reynolds number boundary layers, and recent DNS computations of channel flow support this observation (Iwamoto, 2004). Velocity correlation methods derived from stationary probes tend to underestimate the streamwise length of a meandering streamwise vortex, because only limited portions of such a vortex intersect the probe. The persistence distance of the near-wall vortices is difficult to evaluate for the same reasons. Probably the most complete description of their formation is given by Schoppa and Hussain (1997). As Cantwell points out, even if the low-speed streaks are generated directly by pairs of counterrotating vortices, it does not necessarily follow that the two must have the same streamwise dimension (Smith et al., 1991; Smith and Walker, 1997).

In compressible flow, the only evidence for the behavior of the near-wall structure comes from DNS. Martin (2004), in a study of flat plate boundary layers from Mach 3 to 8, observed a 40% decrease in the streamwise extent of the near-wall streaks with Mach number (as a fraction of δ), and a 20% decrease in spanwise spacing (in terms of ν_w/u_τ). These decreases may be due to the spatial variation in the viscous length, because the rapid variations in temperature near the wall cause significant changes in the local density and viscosity. The fact that an increasing wall temperature had a similar effect on the streaks supports this suggestion.

The convection velocities of the various types of near-wall structures are fairly well established, at least in subsonic flows, and the values represent data from a wide range of studies, primarily correlation based. For example, the average convection velocity of the near-wall streamwise vortices is probably close to the local mean velocity, because the low- and high-speed streaks move at about 50% and 150% of the local mean velocity, respectively (Cantwell, 1981).

In contrast, the scaling of the mean bursting period, T_b (or mean bursting

frequency, $f_b \sim 1/T_b$) is still controversial. Initially, Kline et al. suggested that, because the bursting process is a wall-layer phenomenon, T_b should scale with inner variables. Subsequent research has provided many conflicting results. Rao et al. (1971), working in a turbulent boundary layer in the range $600 < Re_\theta < 9000$, concluded that outer scaling is appropriate, and that $T_b U_e/\delta \approx 5$ (or $T_b U_e/\delta^* \approx 30$), independent of Reynolds number. Alfredsson et al. (1988), working in a fully developed channel flow in the range $13{,}800 < Re_c < 123{,}000$ (Re_c based on channel height and centerline velocity), found that T_b was independent of Reynolds number when nondimensionalized by a mixed time scale equal to the geometric mean of the inner and outer time scales. Thus, three different scalings for T_b (and thus f_b) have been proposed, and the issue has not yet been resolved.

The scaling of T_b is important in its implications for the dynamics of the turbulent boundary layer. If T_b scales on inner variables, it suggests that the inner layer controls the dynamics of the boundary layer, and the outer layer structure may be merely the debris of the bursting process. Alternatively, if T_b follows outer scaling, it implies that the bursting process is controlled or modulated by (and may be responding passively to) the outer layer structure. If T_b scales on mixed variables, it implies an important mutual interaction between the inner and outer structure.

There are many reasons for the discrepancy among the various results. Measurement errors are important, in that spatial-averaging effects will lead to an underestimate of f_b (Blackwelder and Haritonidis, 1983). More important, in order to measure the bursting period, it is necessary to devise a criterion for detecting the bursting process. Visual methods, as used by Kline et al., Corino and Brodkey, and Kim et al., are limited to very low Reynolds numbers. Therefore, Lu and Willmarth (1973) introduced the u'-level method, in which low values of u', relative to the mean, were used to detect ejections, and high levels of u' were used to detect sweeps. Wallace et al. (1972) and Lu and Willmarth (1973) proposed splitting the u'–v' velocity plane into four quadrants, as shown in Figure 8.24. Instantaneous values of $-u'v'$ can then be associated with a certain quadrant and a corresponding event (see also Antonia (1971)).

Blackwelder and Kaplan (1976) developed an alternative method, the Variable Interval Time Averaging (VITA) technique, whereby the variance of the velocity u' is computed over a short time interval. When the short time variance exceeds a preset threshold level, an event is said to have occurred. The goal of these detection schemes is to identify segments of the velocity signal that correspond to events of interest (for example, ejections and sweeps), and to analyze these segments separately from the remaining signal by conditional sampling and averaging.

All detection methods are, to some extent, subjective because they require the user to choose threshold levels and/or averaging times. Willmarth and

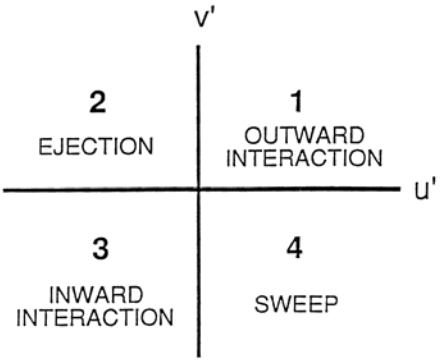

Figure 8.24. The four quadrants of the u'–v' plane, and the common terms for the events corresponding to each quadrant. (Figure from Robinson (1991b), with the author's permission.)

Sharma (1984) found that the bursting period determined using the VITA technique is highly sensitive to the threshold level and the averaging time. When the threshold level was changed by 5%, the measured bursting frequency changed by 40%, and a 20% change in the averaging time resulted in a 15% change in measured bursting frequency. More disturbing is the fact that it is not certain what relationship exists between the detected events and the actual events occurring during the bursting process. Bogard and Tiederman (1986, 1987) evaluated several detection methods and found that different methods could yield values of T_b which differed by an order of magnitude. They also found that different techniques detected different phases of the bursting process. Corino and Brodkey (1969) had already observed that more than one ejection may occur during a single burst, leading to further variations among the reported results. Reynolds number effects may also be important (Shah and Antonia, 1989), and it is possible that the structure of fully developed pipe and channel flows differs from that of turbulent boundary layers because the outer layers have different intermittent characteristics.

8.4.2 Outer Layer Structure

The outer layer is more easily accessible to measurement, and therefore reasonably comprehensive data sets exist for the large-scale structure of subsonic and supersonic flows. The current state of knowledge concerning compressible boundary layer structure is derived largely from studies by Robinson (1986); Spina and Smits (1987); Smits et al. (1989); Fernando and Smits (1990), Spina et al. (1991a,b), Donovan et al. (1994), and Bookey et al. (2005b) of flat-plate layers with freestream Mach numbers of approximately 3, and the work by

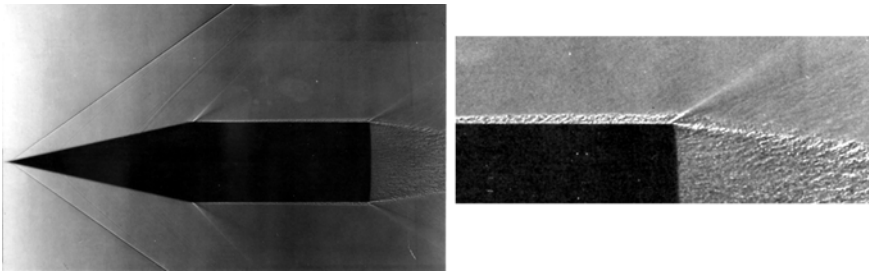

Figure 8.25. Shadowgraph visualizations of the flow over a cone cylinder of 12.5° semi-vertex angle at Mach 1.84. A detail of the flow in the vicinity of the base is shown on the right. (Photograph by A.C. Charters, taken from Van Dyke (1982), with permission.)

Baumgartner et al. (1997) and Bookey et al. (2005a) at Mach 8. These studies were preceded by a pioneering investigation by Owen and Horstman (1972), who made extensive two-point cross-correlation measurements with hot-wires in a Mach 7.2 boundary layer. Most of the results available in the literature were obtained using hot-wire anemometry (with its attendant limitations), with some degree of corroboration at high speed by quantitative flow visualization studies (Smith and Smits, 1988; Cogne et al., 1993; Baumgartner et al., 1997; Bookey et al., 2005a,b).

A characteristic component of the outer layer is the large-scale turbulent *bulge*, also referred to as a *Large-Scale Motion* (LSM). LSMs (Townsend's "main eddies") evolve and decay slowly as they convect downstream, and on average they are inclined to the wall in the downstream direction. Their most identifiable feature is a downstream-sloping shear layer interface between upstream high-speed fluid and downstream low-speed fluid (unfortunately, these structures have been labeled both "fronts" and "backs" in the literature). These interfaces are three-dimensional shear layers that form the upstream side of the largest of the boundary layer eddies, and remain coherent long enough to convect several boundary layer thicknesses downstream. Early shadowgraph images of boundary layers on supersonic bodies of revolution (where the spatial integration is minimized) clearly showed such structures, appearing as marked and regular striations in the layer, leaning downstream at a characteristic angle of 40° to 60° (Figure 8.25). Figure 8.26 shows several LSMs in a subsonic boundary layer, and comparable images for supersonic flow are given in Figure 1.4 and Figure 8.27.

The LSMs are an important feature in that they are responsible for the large-scale transport of turbulence in the outer layer, the growth of the layer by entrainment of initially irrotational flow, and appear to play a role in triggering instabilities in the near-wall region. Up to 40% of the outer layer Reynolds shear stress can be found in the neighborhood of their sloping interfaces (Spina

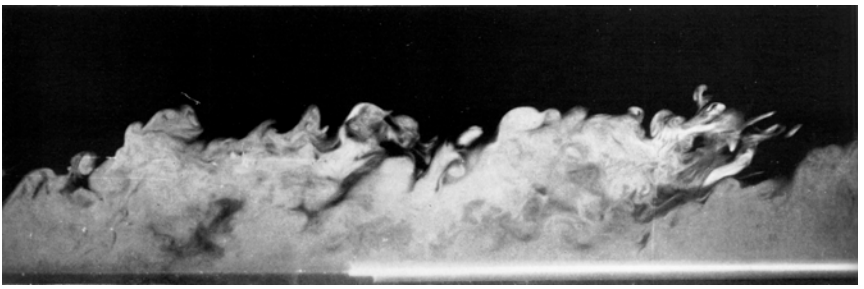

Figure 8.26. Flow visualization of a boundary layer in subsonic flow at $Re_\theta \approx 4000$, obtained by seeding the flow with a fog of oil droplets, and illuminating the flow with a planar laser sheet (Falco, 1977). Flow is from left to right. (Copyright 1977, AIP. Reprinted with permission.)

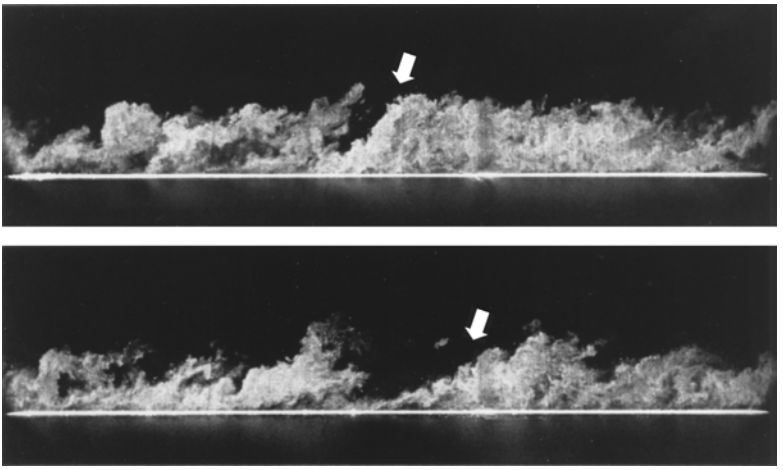

Figure 8.27. Flow visualization of a boundary layer in a Mach 2.82 flow at $Re_\theta = 81{,}190$, obtained by seeding the flow with acetone droplets, and illuminating the flow with a planar laser sheet (the two pictures shown were taken at different times). The flow is from left to right. (Figure from Smith and Smits (1995). Copyright 1995, Springer-Verlag. Reprinted with permission.)

et al., 1991a). Between neighboring bulges, the flow is irrotational, resulting in the intermittent nature of the outer layer. The LSMs vary greatly in size and inclination angle, and their length scales, time scales, convection velocity, and structure angle, as well their characteristic velocity, vorticity, and pressure fields, remain the subject of active research. Furthermore, their Reynolds number and Mach number dependence is not very well understood, although the superficial similarities between the subsonic and supersonic flows is striking

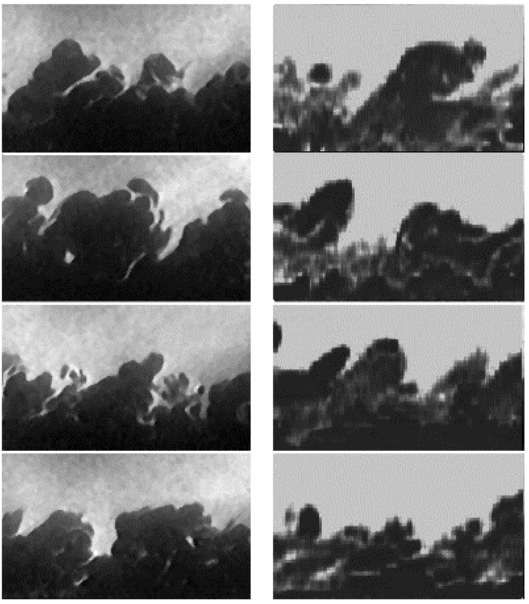

Figure 8.28. Visualizations of flat plate boundary layers. Flow is from left to right. Left: Air at Mach 8, $Re_\theta \approx 3600$ ($\delta^+ \approx 200$), visualized using FRS. Right: Water at Mach 0, $Re_\theta = 700$ ($\delta^+ = 300$), visualized using dye (Delo and Smits, 1997). (Figure from Baumgartner et al. (1997), with the author's permission.)

(compare, for example, Figures 8.26 and 8.27). Even more suggestive is the comparison shown in Figure 8.28, where two low Reynolds number boundary layers, one in a low-speed water channel and the other at Mach 8, are shown side by side.

In contrast to this visual evidence, the hot-wire measurements by Owen et al. (1975) had strongly suggested that the extent of the intermittent zone decreased with Mach number. Part of the difficulty in determining the intermittency (the wallward extent of the entrainment process) is finding an unambiguous criterion for discriminating between turbulent and nonturbulent fluid. Many techniques have been employed, but most methods generate a box-car function by setting a threshold on the turbulence level, or on its first derivative (Antonia, 1971). The most basic output is the intermittency itself, γ, that is, the fraction of the time the flow is turbulent. Another possible method for finding the intermittency is based on the pdf of the turbulence, where γ is measured by the departure of the turbulence from its Gaussian flatness value of 3; that is, $\gamma \equiv 3/F$, where F is the flatness. The flatness distributions for a number of different freestream Mach numbers are shown in

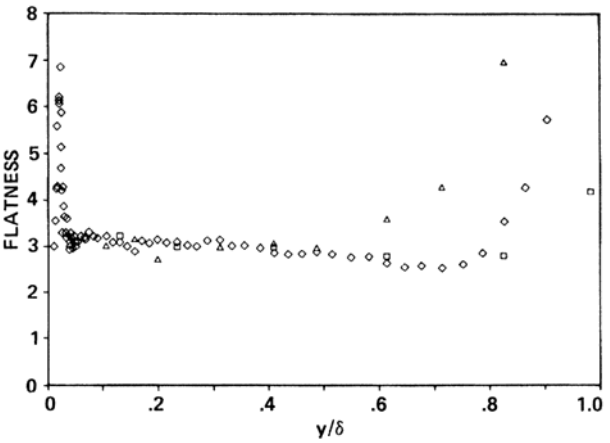

Figure 8.29. Comparison of flatness distributions: □, Owen et al. (1975) (Re_θ = 8500, $M = 7$), based on mass flux; ◇, Robinson (1986) (Re_θ = 15,000, $M = 3.0$, based on mass flux; △, Klebanoff (1955) ($Re_\theta = 7100$, $M \approx 0$), based on velocity. (Figure from Robinson (1986), with the author's permission.)

Figure 8.29. The data display an apparent Mach number dependence, where the onset of intermittency (corresponding to the rise in flatness factor) occurs nearer the boundary layer edge as the Mach number increases. Because the zone of influence of a flow disturbance decreases with Mach number, the intermittent zone could become thinner as the Mach number increases. As already noted, this interpretation is not supported by high-speed flow visualizations, and recent measurements by Baumgartner et al. (1997) and Bookey et al. (2005b), as well as the DNS results of Martin (2004), support the notion that the intermittency does not depend on Mach number to any significant extent (see Figures 8.30 and 8.31).

So far, we have described the LSMs as a unified, large-scale, organized motion. However, considerable evidence now exists to indicate that they possess a rich internal structure, comprising "typical eddies," and horseshoe or hairpin eddies, and that the LSMs may well be formed by well-organized "packets" of hairpin eddies that are originally attached to the wall, and subsequently become detached as vorticity cancellation and viscous effects take place. These eddy structures are discussed in detail in Section 8.7.

8.5 Correlations and Ensemble Averages

A common method for investigating the large-scale structure is multiple-point measurements of one or more flow variables, typically velocity, wall pressure,

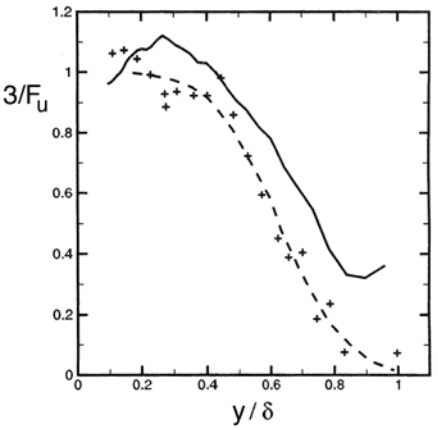

Figure 8.30. Comparison of intermittency distributions based on flatness of the streamwise velocity: +, Eléna and Lacharme (1988) ($Re_\theta = 5650$, $M = 2.32$, LDV); ———, Martin (2004) ($Re_\theta = 4452$, $M = 2.32$, DNS); – – –, Klebanoff (1955) ($Re_\theta = 7100$, $M \approx 0$, HWA). (Figure from Martin (2004), with the author's permission.)

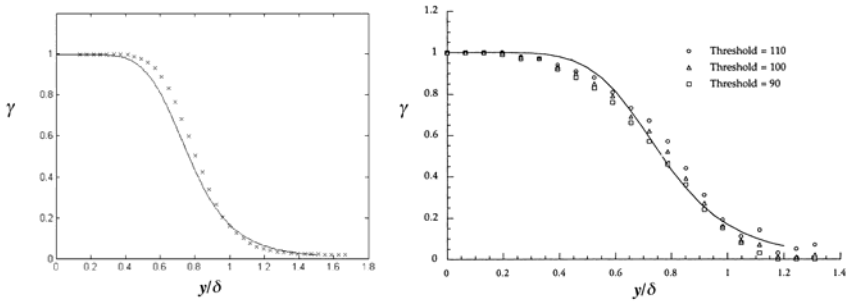

Figure 8.31. Intermittency distributions. Left: ×, Baumgartner et al. (1997) ($Re_\theta = 3600$, $M = 8$, FRS); ———, Klebanoff (1955) ($Re_\theta = 7100$, $M \approx 0$, HWA). Right: Bookey et al. (2005b) ($Re_\theta = 2400$, $M = 2.9$), FRS. (Figures adapted from Baumgartner et al. (1997) and Bookey et al. (2005b), with the authors' permission.)

and wall shear stress. The data are then analyzed in the context of space-time correlations. Space-time correlations generally have a single well-defined peak, which occurs at $\tau = \tau_{max}$, the optimum time delay, which is usually nonzero.

Favre et al. (1957, 1958) pioneered the use of velocity space-time correlations. Their results, for Re_θ values of about 1400 and 2700, showed that the fluctuating velocities in the outer layer are correlated over distances comparable to the boundary layer thickness in the spanwise and wall-normal directions,

and over several boundary layer thicknesses in the streamwise direction. The space-time correlations for optimum time delay also showed that, in the outer layer, structures are convected downstream for a distance of $O(10\delta)$ before decaying. Nearer the wall, the structures decay more rapidly. Sternberg (1967) noted that Favre et al.'s results also indicate that the large eddies are inclined to the wall in the downstream direction.

In a later paper, Favre et al. (1967) used space-time correlations to measure convection velocities of the large-scale motions in a turbulent boundary layer with $Re_\theta \approx 8700$. To complement their broadband results, they bandpass filtered the data to measure the convection velocities of structures within a narrow range of scales. They found that the smallest scales convect at about the local mean velocity throughout the boundary layer. For $y/\delta > 0.2$, large-scale structures convect at speeds less than the local mean velocity, and the convection velocity decreases with scale. For $y/\delta < 0.2$, the opposite behavior is observed. At $y/\delta \approx 0.2$, all scales convect at the local mean velocity. This behavior could be explained as follows. A large structure will extend across a significant fraction of the boundary layer, and will convect at a speed that is a weighted average of the local mean velocity acting over the vertical span of the structure. This convection velocity will be greater than the local mean near the wall, and less than the local mean in the outer layer. The greater the vertical extent of the structure, the greater will be this effect. Based upon space-time correlations of wall pressure fluctuations, Corcos (1963) and Tu and Willmarth (1966) reached similar conclusions regarding the difference in convection velocity between large- and small-scale structures. Spina et al. (1991b) obtained similar results for the convection velocity distribution in a compressible flow (see Figure 8.32).

Using conditional averaging techniques based on the intermittency, Kovasznay et al. (1970) and Blackwelder and Kovasznay (1972) discovered a stagnation point on the back (upstream) side of the turbulent bulges in a subsonic boundary layer. Because the bulges convect at a speed less than the freestream velocity, the high-speed freestream fluid in the regions between the bulges will impinge on the backs of the bulges, resulting in a stagnation point in the convected frame of reference, as shown in Figure 8.33. Similar to the results of Favre et al. (1957, 1958) Kovasznay et al. found that isocontours of the space-time correlations of the streamwise velocity were elongated in the streamwise direction and spanned the entire boundary layer thickness, and that the large eddies lean downstream (see Figure 8.34). The contours were generated by correlating the velocity measured by a probe at a fixed point in the middle of the boundary layer with the velocity measured by a probe that was traversed in both the y- and z-directions while maintaining a constant longitudinal probe separation of 3.8δ. The results indicate that the large eddies are inclined with an average angle of approximately 16°. At the location of the fixed point, the streamwise extent of the correlations is about 0.4δ (based on a minimum

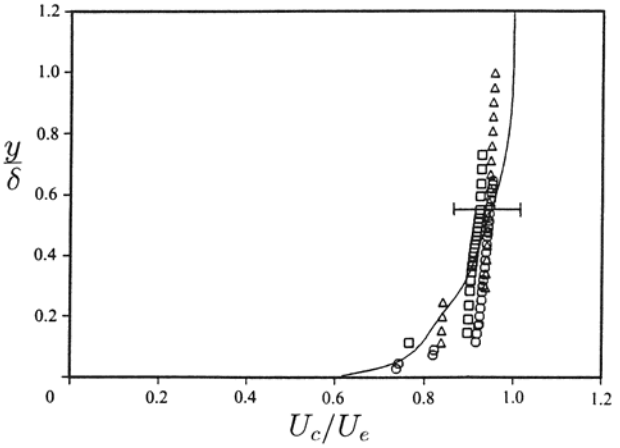

Figure 8.32. Broadband convection velocity in a turbulent boundary layer at $Re_\theta = 81{,}000$ and $M = 2.9$, based on measurements with three different streamwise probe separations. $\xi_x/\delta = 0.11$ □ ; 0.16 ○; 0.18 △. (Figure from Spina et al. (1991a). Copyright 1991, Cambridge University Press. Reprinted with permission.)

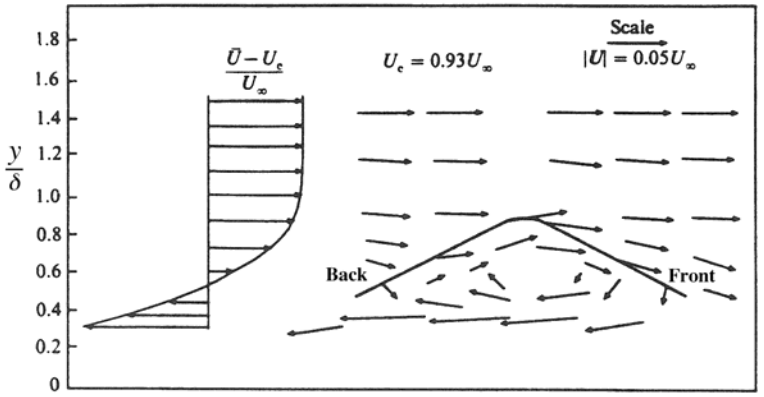

Figure 8.33. Schematic of the flowfield within and surrounding a large-scale motion in a turbulent boundary layer, according to Blackwelder and Kovasznay (1972). (Figure from Spina et al. (1991a). Copyright 1991, Cambridge University Press. Reprinted with permission.)

correlation value of 0.5).

Murlis et al. (1982) used hot-wire anemometry and temperature-tagging methods to study the effect of Reynolds number on boundary layer structure

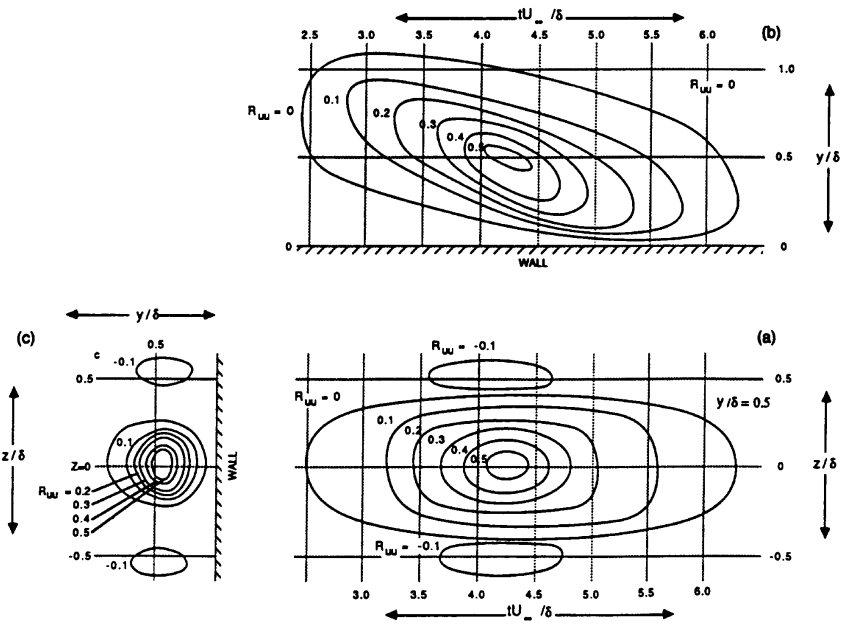

Figure 8.34. Isocorrelation contours of space-time correlations of the streamwise velocity component measured by Kovasznay et al. (1970). (a) x–z plane, (b) x–y plane, and (c) y–z plane. The position of one probe was fixed at $y/\delta = 0.5$. (Copyright 1987, Cambridge University Press. Reprinted with permission.)

for $791 < Re_\theta < 4750$. They found that the intermittency profile is essentially independent of Reynolds number. However, the average length of zones of turbulent motion was found to decrease with increasing Reynolds number up to $Re_\theta \approx 5000$. Their data suggested that, beyond this Reynolds number, the turbulent zone length remained constant. Similarly, Antonia et al. (1990a,b), using what they called a "window average gradient" detection scheme, found that the average period between detected events in the outer layer is independent of Reynolds number when scaled on outer variables, and it has a value of $\approx 2.5\delta/U_e$. This value is similar to that obtained by Corrsin and Kistler (1955) and Ueda and Hinze (1975), as noted by Falco (1977). Conditionally averaged isovorticity contours were observed to extend further from the wall and have a larger inclination angle (they were more upright) at lower Reynolds numbers, and the contribution of the organized motion to the turbulence stresses decreased as the Reynolds number increased.

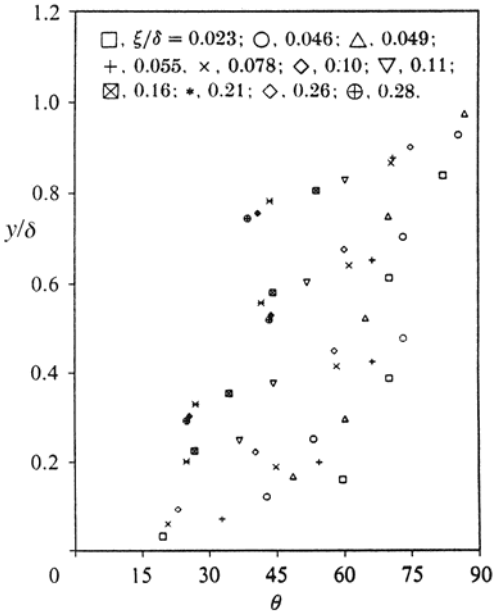

Figure 8.35. Broadband structure angle in a subsonic boundary layer, as a function of probe separation distance. (Figure from Alving et al. (1990). Copyright 1990, Cambridge University Press. Reprinted with permission.)

8.5.1 Structure Angle

Alving and Smits (1990) and Alving et al. (1990) measured the broadband structure angle of the LSMs by using two probes separated by a distance ξ_y in the wall-normal direction. The *structure angle* was defined by $\theta = \tan^{-1}(\xi_y/U_c\tau_{max})$, where U_c is the convection velocity (assumed to be equal to the local mean velocity) and τ_{max} is the time delay to the maximum in the space-time correlation. The results given in Figure 8.35 indicate that θ is a strong function of probe separation when ξ_y is small. It appears, however, that θ reaches a limit as ξ_y increases, where it becomes independent of probe separation. The angles in the middle of the layer are about 30°, considerably higher than the values found by Brown and Thomas (1977) and Kovasznay et al. (1970). Perry et al. (1992) measured structure angles by fixing the wall-normal separation of two probes and varying the streamwise separation until the value of the cross-correlation of the signals from the two probes attained a peak. This method has the advantage of not depending on the validity of Taylor's hypothesis. The results agreed well with the data of Alving et al. (1990), for which the probes were separated in only the wall-normal direction

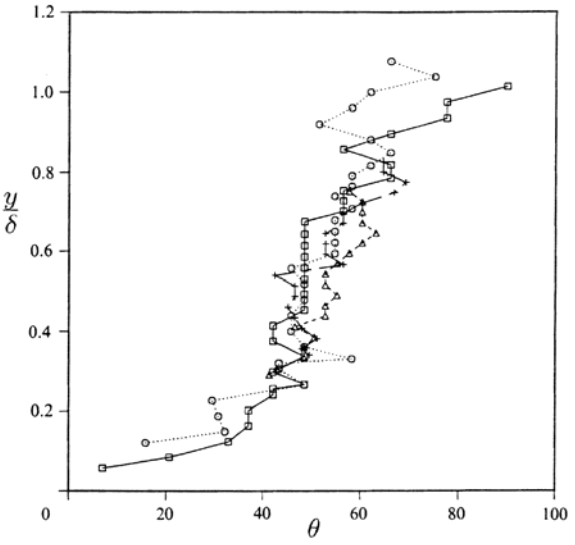

Figure 8.36. Broadband structure angle found using two hot-wire probes with different wall-normal separations. ξ_y/δ = 0.09 ———— □; 0.21 ----------○, 0.30 ---------△; 0.40 ——-——-+. (Figure from Spina et al. (1991a). Copyright 1991, Cambridge University Press. Reprinted with permission.)

and Taylor's hypothesis was used.

Hot-wire and flow visualizations show that the sloping delta-scale structures convect downstream at approximately 90% of the freestream velocity (slightly greater than for similar structures in low Reynolds number, incompressible turbulent boundary layers), and at Mach 2.9 persist for at least four boundary layer thicknesses downstream (and probably much farther) (Spina et al., 1991b). The average angle at which the sharp interfaces lean downstream ranges from 45° to 60° (with a standard deviation of approximately 20°) across most of the boundary layer, with a decrease near the wall and an increase near the boundary layer edge. The measured value of the structure angle is strongly dependent on measurement technique, although one method in current favor employs two hot-wires, separated by a fixed distance in y of 0.1 to 0.3δ, with both traversed across the layer. Structure angles measured using this technique in subsonic, low Reynolds number turbulent boundary layers are somewhat lower than those for Mach 3, high Reynolds number layers (see Figures 8.35 and 8.36). As indicated earlier, it seems likely that increasing Reynolds number decreases the structure angle, and increasing Mach number increases the structure angle.

Space-time correlation measurements by Smith (1994) at Reynolds numbers in the range $4600 \leq Re_\theta \leq 13{,}200$ showed that the broadband convection

velocity and the decay of the large scales with increasing time delay were only weakly dependent on Reynolds number when scaled on outer layer variables (U_e and δ). However, isocorrelation contours indicated that the streamwise length scales increased with Reynolds number, in agreement with the results by Liu et al. (1991) in a fully developed channel flow. Furthermore, space-time correlations in the wall-normal direction revealed that the broadband structure angle *decreased* by about 10° over the same range in Re_θ. Isocorrelation contour maps (Figures 8.37 and 8.38) showed an *increase* of between 30 and 60% in the streamwise length scale over the same Reynolds number range, and this behavior may be related to the decrease in the structure angle. The spanwise length scale showed comparatively little variation.

These subsonic results provide an interesting contrast to the results obtained by Spina et al. (1991a) in a Mach 3 boundary layer with $Re_\theta = 80{,}000$ (see Figure 8.39). In the supersonic flow, the streamwise length scales were two to three times *smaller* than in the subsonic flow, and the structure angles were about 10° *larger*.[1] The spanwise scales were almost independent of the Mach number. Now, the smaller streamwise scale is in accordance with the more upright orientation of the structure, but the trend with Reynolds number for subsonic flows does not seem to hold for supersonic flows. It seems that the streamwise length scale and the structure angle depend on the Mach number and the Reynolds number. This seems to be the most significant structural difference between the two flows yet found, and as indicated earlier Reynolds number and Mach number appear to be important. Increasing Reynolds number will increase the streamwise scales, whereas increasing Mach number will decrease them. Otherwise, the structural model for the large-scale motions in a supersonic flow is very similar to that derived from studies of subsonic flows, as can be seen by comparing Figures 8.33 and 8.40.

Because the influence of compressibility on the large-scale turbulent boundary layer motions seems to be subtle, explanations for the observed differences between low- and high-speed boundary layer structure are mostly speculative. Density gradient effects are known to play a significant role in turbulent shear layers, but these effects are most likely to influence the near-wall region of the wall layer, out of reach of standard measurement techniques. Parallels have also been drawn between the 45-degree slope of the interfacial structures in supersonic boundary layers and that of the hairpin-vortex structure observed in incompressible boundary layers. Insufficient evidence exists to support either side of this comparison, however. More conclusive results concerning compressibility effects on large-scale structure require higher Mach number investigations.

For boundary layers with freestream Mach numbers above 5, the near-wall region is more likely to show significant departures from known incompress-

[1]Baumgartner (1997) found similar results based on FRS measurements in a Mach 8 boundary layer with $Re_\theta = 3600$.

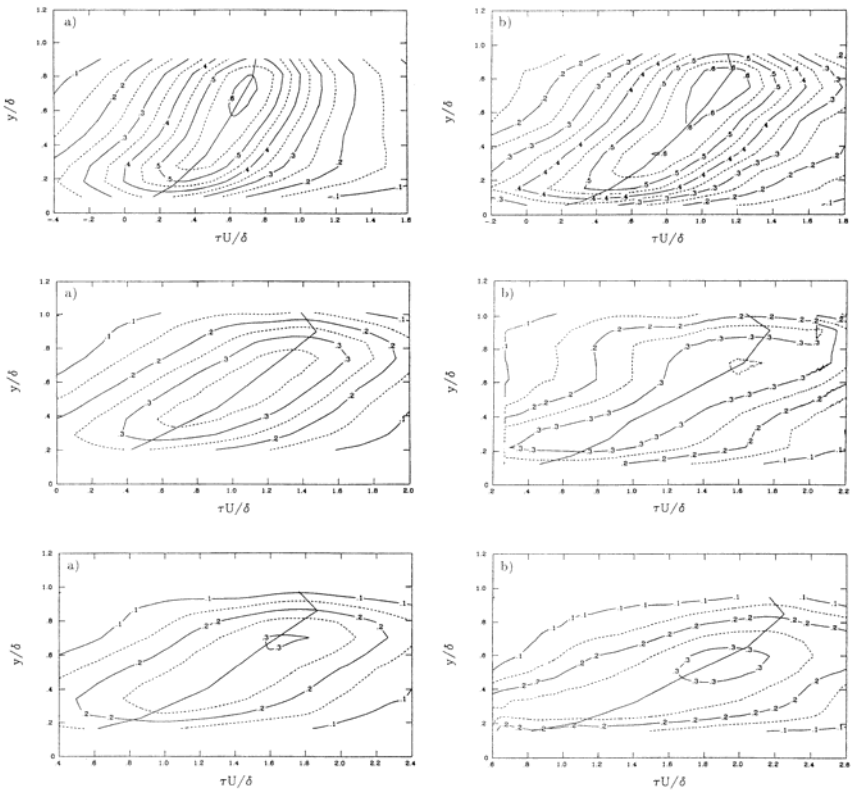

Figure 8.37. Isocorrelation contour maps in the x–y plane, as measured by Smith (1994), in a subsonic turbulent boundary layer at $Re_\theta = 4981$ (left) and 13,052 (right) using different wall-normal probe separations: (a) $\xi_y/\delta \approx 0.1$; (b) $\xi_y/\delta \approx 0.2$; (c) $\xi_y/\delta \approx 0.3$. (Figure from Smith (1994), with the author's permission.)

ible structure. The viscous sublayer for hypersonic boundary layers is likely to be much more quiescent than for incompressible flows (although pressure fluctuations will be imposed from above), and it may not display the familiar streaky structure. Because the mass flux near the wall is very low for high Mach numbers, the buffer region may not be the dominant region for turbulence production, as in subsonic boundary layers (note that hypersonic laminar boundary layers undergo transition by disturbances spreading inward from the outer layer). Further investigation will depend on the development and application of nonintrusive measurement techniques to the near-wall regions of hypersonic boundary layers.

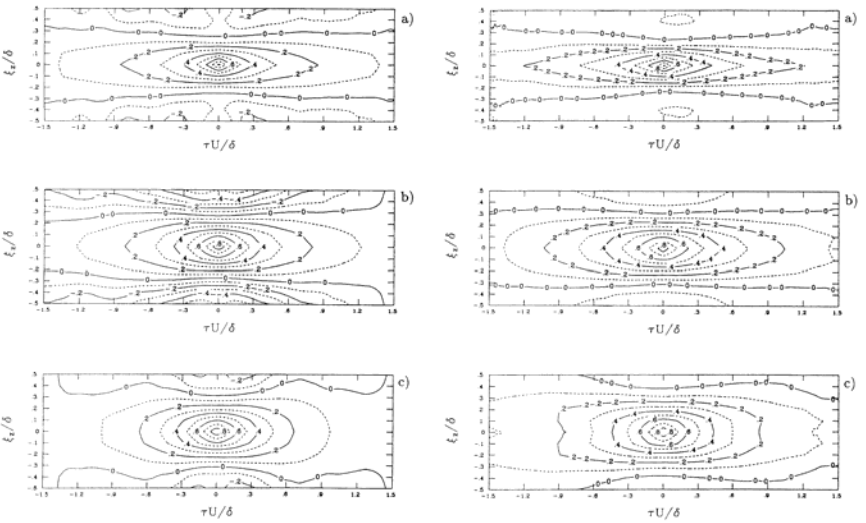

Figure 8.38. Isocorrelation contour maps in the x–z plane, as measured by Smith (1994), in a subsonic turbulent boundary layer at (a) $y/\delta = 0.09$, (b) 0.42, (c) 0.80. Left: $Re_\theta \approx 4600$; right: $Re_\theta \approx 13{,}200$. (Figure from Smith (1994), with the author's permission.)

Finally, we note that the rate of decay of the large-scale motions, as measured by the rate at which the peak in the space-time correlation decays with distance, appears to decrease significantly with the Mach number. For example, the distance over which the peak decreased to half its original level differs by an order of magnitude in the experiments by Favre (1957, 1958) at Mach 0.04 and Owen and Horstman (1972) at Mach 7 when scaled by δ. A better scaling for the rate of decay may be the time scale of the energy-containing eddies, Λ/u'. Λ and u' both decrease with Mach number so that their ratio remains approximately constant. This result may in turn suggest that the decrease in the streamwise length scales with Mach number simply reflects the fact that the time scale of the large eddies remains constant as the absolute fluctuation level decreases. The more complex scaling arguments presented by Smith and Smits (1991b) to explain the experimental observations may therefore not be necessary.

8.6 Integral Scales

Experimentally, the integral scales are usually deduced from one-point hot-wire measurements by using Taylor's hypothesis. Even when measurements of two-point correlations are available in high-speed flows (see, for example,

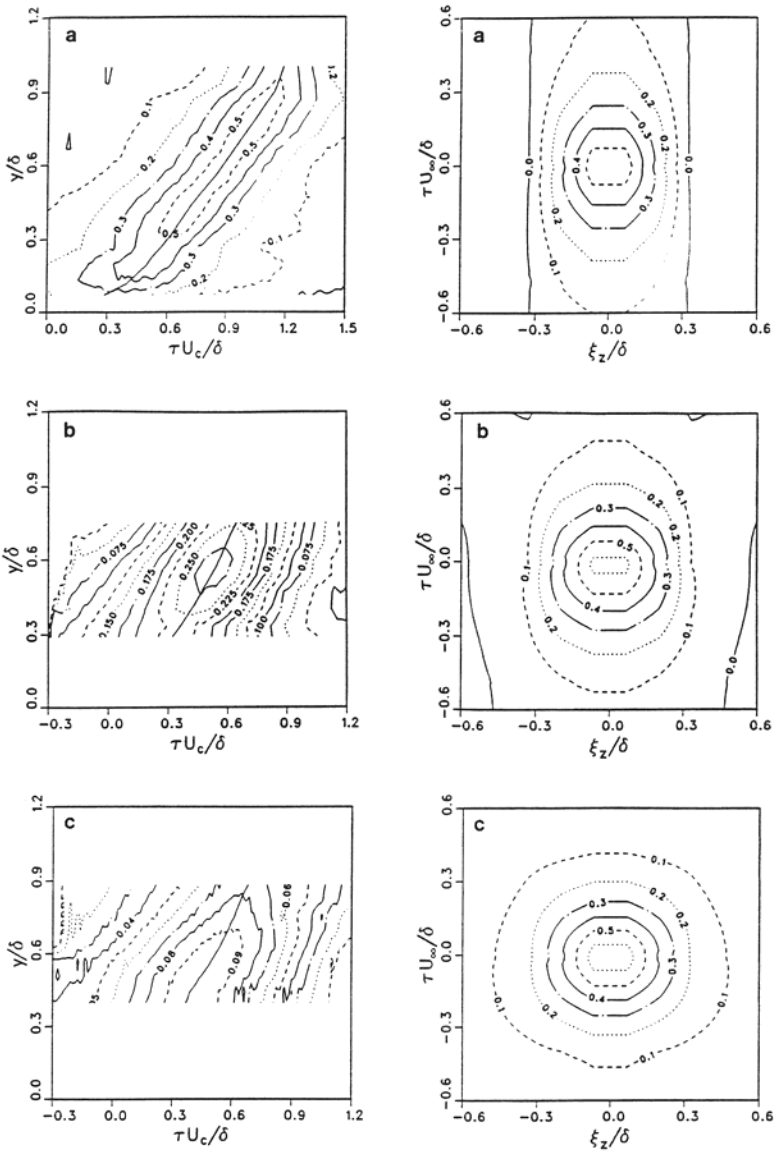

Figure 8.39. Isocorrelation contour maps measured by Spina (1988), in a turbulent boundary layer at $Re_\theta = 81{,}000$ and $M = 2.9$. The figure on the left shows the results in the x–y plane using different wall-normal probe separations: (a) $\xi_y/\delta = 0.09$; (b) $\xi_y/\delta = 0.30$; (c) $\xi_y/\delta = 0.51$. The figure on the right shows the results in the x–z plane at three positions in the boundary layer: (a) $y/\delta = 0.20$; (b) $y/\delta = 0.51$; (c) $y/\delta = 0.82$. (Figure adapted from Spina (1988), with the author's permission.)

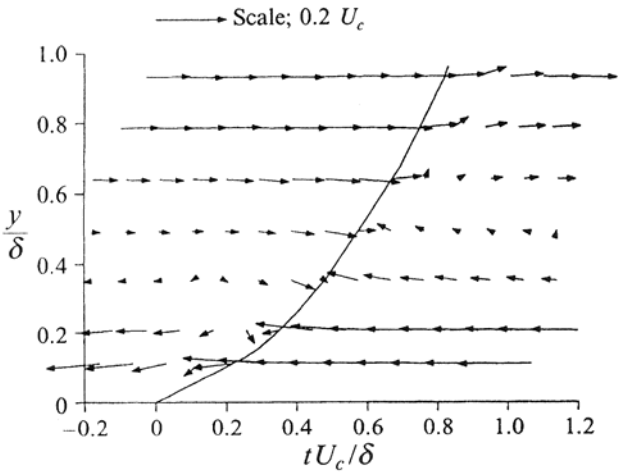

Figure 8.40. Ensemble averaged view of the large-scale motions in a Mach 2.9 boundary layer. (Figure from Spina et al. (1991a). Copyright 1991, Cambridge University Press. Reprinted with permission.)

Spina and Smits (1987) and Robinson (1986)), it is often difficult to determine integral scales from the data. The type of data that is available also depends on the measurement technique. For instance, when Constant Current Anemometers (CCA) are used, time histories are generally not measured, but spectral data for u' and T' can be obtained directly by processing the signal with the fluctuation diagram technique to separate the contributions of u' and T' (see Fulachier (1972), Bestion (1982), Debiève et al. (1982, 1983), Bestion et al. (1983), and Audiffren (1993)). Bestion and Audiffren showed that for an adiabatic flat plate boundary layer at a Mach number of 2.3 the shapes of the spectra of $(\rho u)'$ and u' are practically the same, but they differ considerably from the spectrum of T_0'. Therefore, when anemometers are operated with a single overheat, a sufficiently high value of the resistance should be chosen to minimize the contribution of T_0' and to obtain a signal proportional to $(\rho u)'$. When Constant Temperature hot-wire Anemometers (CTA) are used at a high overheat ratio, the measured signal is almost exactly proportional to $(\rho u)'$, which in turn gives spectral information on u'. Such data can be inaccurate at low wave numbers. The spectral measurements of velocity and temperature performed with a CCA in adiabatic boundary layers by Morkovin (1962), Bestion (1982), and Audiffren (1993) show that the ratio $(u'/U)/(T'/T)$ at low frequencies is not a constant, and that the magnitude of the spectral correlation coefficient $R_{uT}(f)$ increases to unity at zero frequency. This may be the cause for the differences in the shapes of the spectra for u' and $(\rho u)'$ at low frequencies, depending on the Mach number. For higher frequencies, the ratio

$(u'/U)/(T'/T)$ and the correlation coefficient are approximately constant, and the spectra are nearly proportional to each other.

The classical integral scale can be determined from one-point measurements by integrating the autocorrelation coefficient of u'. It is necessary to define the domain of integration, because the autocorrelation can become negative. When using hot-wire anemometry in supersonic flows, this question can be complicated by possible "strain-gauge" effects. These effects can cause peaks in the spectrum, which may be acceptable for measurements of the overall stress or the turbulence energy because the integral contribution is usually small, but they can cause spurious oscillations in the autocorrelations and make the estimates of the integral scale inaccurate.

Alternatively, the integral scale can be determined by finding the value of the energy spectrum at zero frequency. However, because the signal is usually filtered with a highpass filter, it has zero mean and its spectrum has a zero value at zero frequency. The integral scale must then be found by extrapolating the spectrum to zero frequency. In practice, the value at a frequency slightly larger than the limit of the highpass filter is taken as the best estimate. It is generally difficult to measure these low frequencies because the spectra of u' and of $(\rho u)'$ may be different at very low frequencies, the measurements can be affected by noise in the power supply, and by the peculiarities of the wind tunnel, such as acoustic resonances.

For these reasons, an additional scale has also been used. Because we expect that the spectra have a region of k_1^{-1} dependence in the logarithmic zone, $E(k_1)$ varies as k_1^{-1}, and $k_1 E(k_1)$ is constant or presents a maximum. Here we have chosen the wave number for which this maximum occurs as the (inverse of the) characteristic space scale. This probably has a clearer physical meaning than the integral scale, since for the incompressible part of the fluctuating motion it characterizes the eddies extracting energy from the mean field. As indicated earlier, experimentalists commonly measure frequency spectra, so that a characteristic frequency is measured, and then a length scale is deduced using Taylor's hypothesis. There is usually a considerable amount of scatter because the location of the maximum is not always well defined. For the data considered here, a maximum was generally found in the external layer, but in the logarithmic zone of the subsonic boundary layer the spectra were frequently "double-humped" and the maximum was difficult to determine. Such shapes were also mentioned by Perry et al. (1986) who interpreted them to mean that Taylor's hypothesis failed for low frequencies. Uddin (1994) noted that the bump at low wave number became more prominent at higher Reynolds numbers (see also Smith (1994)). These double-humped profiles lead to some difficulty in determining the length scale, and it is sometimes necessary to discard points in the log-law region of the subsonic boundary layer profiles. However, the higher frequency bump typically corresponds to scales comparable to the scales of the outer layer, and the other maximum

Authors	M	$R_\theta - R_{\delta 2}$	Measurement method	Remarks
Klebanoff (1954)	0.044	7000	CCA	
Fulachier (1972)	0.035	4750	CCA	
Fernholz et al. (1994)	0.06 and 0.17	20000 and 60000	CTA	
Spina and Smits (1994)	2.89	80000 – 40000	CTA	Scales estimated from spectra of $(\rho u)'$
Bestion (1982) Debiève (1983)	2.3	4200 – 2900	CCA	Spectra of u' (fluctuation diagram technique)
Bestion et al. (1983)	1.8 and	5000 – 3500	CCA	Spectra of u' (fluctuation diagram technique)
Audiffren (1993) Audiffren and Debiève (1995)	2.2	6300 – 3800	CCA	Spectra of u' (fluctuation diagram technique)
McGinley et al. (1994)	11	12400 – 1115 6500 – 633	CTA	Spectra of $(\rho u)'$

Table 8.1. Sources for spectral data. (Adapted from Dussauge and Smits (1995).)

occurs at frequencies an order of magnitude lower, corresponding to length scales five to ten times larger than the outer layer scales.

The values of the integral scale Λ obtained from the data sets listed in Table 8.1 are given in Figure 8.41. Outer layer scaling was used, because most of the data were obtained in that region. Plotting the data in inner layer variables does not alter the conclusions. The data points from Smits and Dussauge (1989) were deduced from autocorrelations in a way that may underestimate the integral scale, due to a lack of experimental points for large time delays. The boundary layer thickness was found from the profiles of total pressure (as recommended by Fernholz and Finley (1980)). Choosing a boundary layer thickness based on $0.99U_e$ would make some difference in the magnitude of Λ/δ at Mach 3: in this experiment, the integral scale would be a little closer to its subsonic value. It would also significantly increase Λ/δ for the hypersonic experiment by McGinley et al. (1994), but in this case, the mean profiles indicate that the traditional choice based on $0.99U_e$ would be rather unphysical. In any case, a first result appears very clearly: the subsonic data indicate that in the external layer, Λ is about 0.5δ in subsonic flows, but it is only about half that value in supersonic layers. The hypersonic data of McGinley et al. (1994) indicate a very low value, about 0.2δ, for $R_{\delta 2} = 1115$, but larger values at the lower Reynolds number. In this case, the spectra

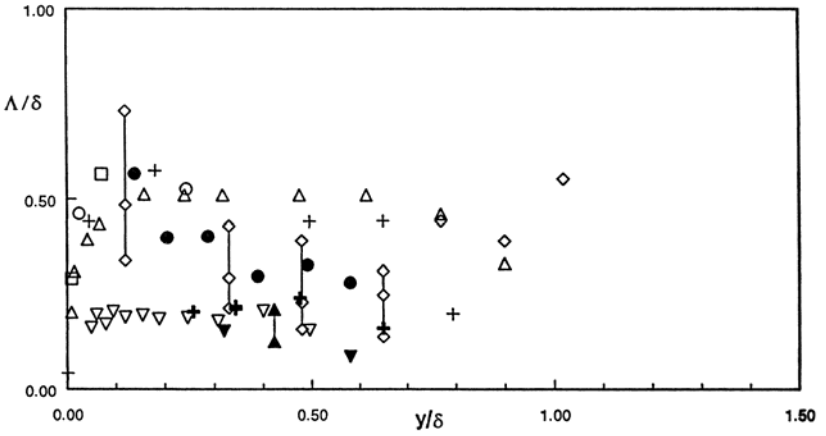

Figure 8.41. Integral scales in turbulent boundary layers. Subsonic data: +, Klebanoff (1955); △, Fulachier (1972); ○ $R_{\delta 2}$ = 20,900, Fernholz et al. (1995); □ $R_{\delta 2}$ = 57,720, Fernholz et al. (1995). Supersonic data: +, Debiève (1983); △, Bestion et al. (1983); ○, Spina and Smits (1987); ▽, Audiffren (1993); ◇ $R_{\delta 2}$ = 633, McGinley et al. (1994); ▽ $R_{\delta 2}$ = 1115, McGinley et al. (1994). (Figure from Dussauge and Smits (1995), with the authors' permission.)

at low frequency reveal peaks and bumps that preclude an accurate estimate of the integral scale. In fact, the lower limit of the error bar overlaps the other high-speed data. The large variation could be due to the remnants of transition. In the data by Spina and Smits, the point at $y/\delta = 0.1$ has an integral scale nearly equal to the subsonic value. This is due to the significant slope in the spectrum, observed at low frequency, where the spectra of u' and $(\rho u)'$ are perhaps not proportional, as discussed above. In spite of this trend, the integral scales at Mach 2.9 in the middle of the layer are significantly below the subsonic results. The results are independent of Reynolds number, within the experimental accuracy. Note that Demetriades and Martindale (1983) in a boundary layer on a flat plate at Mach 3 report measuring an integral scale of 0.28δ, also considerably smaller than that found in subsonic flows.

The production scales L are given in Figure 8.42. The Reynolds numbers in the subsonic and supersonic cases cover comparable ranges, except perhaps for the hypersonic data. It is clear that the production range is shifted to higher frequencies in supersonic flows. It should be emphasized that the limited spatial resolution of the wires probably precludes any accurate determination of the $-5/3$ law in the supersonic data, and tends to shift the maximum of $fE(f)$ to lower frequencies. If such systematic errors are significant, the values measured in high-speed flows are probably overestimated, reinforcing the notion that the scales are reduced with increasing Mach number.

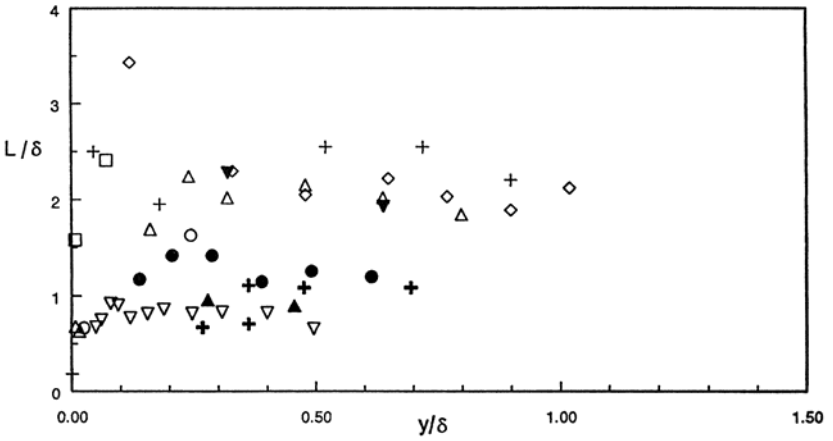

Figure 8.42. Production scales in turbulent boundary layers. Symbols as in Figure 8.41. (Figure from Dussauge and Smits (1995), with the authors' permission.)

It appears that the production scale L follows the same trends as Λ, and that $L \approx 2\Lambda$. That is, L is about 2δ for low-speed boundary layers, and about δ in high-speed boundary layers. The measurements of Morkovin and Phinney, reported by Morkovin (1962), suggested the same trend for the production scales. Again, plotting these data in inner-layer variables does not change the differences between the subsonic and supersonic data. The only discrepancy is found in the Mach 11 boundary layer, but several reasons can be found for this departure. First, the boundary layer is probably not fully turbulent, at least at the lower Reynolds number. Second, it is not clear that the velocity and mass-flux spectra are proportional to each other at this Mach number. Third, the conclusions drawn from the power law analysis are probably not valid if strong compressibility effects are present. Fourth, the change in the shape of the spectra may indicate a modification of the turbulence structure. In hypersonic boundary layers, most of the mass flux occurs near the external edge of the layer and the mass flux profiles have an inflexion point. This suggests that the external layer can behave more like a mixing layer than a classical boundary layer. Such free shear flows are known to contain turbulent structures of large spatial extent, with the production scales being several boundary layer thicknesses in size. This would be consistent with the surprisingly high level of energy observed at low frequencies in the present Mach 11 experiments.

So it seems that the apparent size of the energetic eddies in the longitudinal direction, deduced from measurements of u' or $(\rho u)'$ in zero pressure gradient boundary layers, decreases with increasing Mach number whatever the experimental method. This trend can also be illustrated by using another

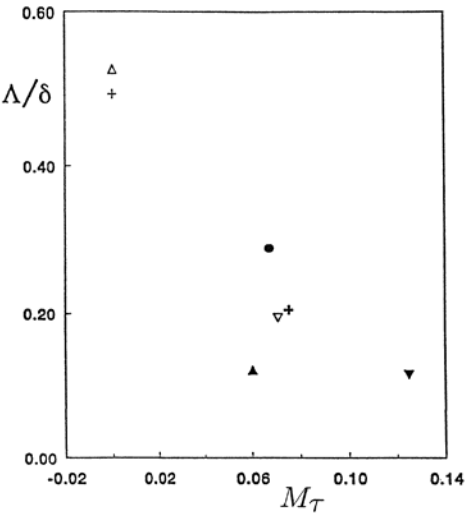

Figure 8.43. Evolution of the integral scale as a function of the friction Mach number. Symbols as in Figure 8.41. (Figure from Dussauge and Smits (1995), with the authors' permission.)

representation. If we assume that the friction Mach number can be used to characterize compressibility in turbulent boundary layers, then we can write $M_\tau^2 = C_f M_e^2/2$. That is, M_τ depends on Mach and Reynolds number. The average value of L/δ in the outer layer is shown as a function of M_τ in Figure 8.43. The results obtained at $M_e = 2.3$ and 2.89 have nearly the same values of M_τ and L/δ, and they agree on the average value of L/δ. The hypersonic results by McGinley et al. have a value of M_τ only a little larger than 0.1, but they indicate a further decrease in the production scale.

This change in typical frequencies or time scales can be attributed either to variations in the convection velocity or variations in the spatial scales. Measurements of convection velocity by Spina and Smits (1987) in a high Reynolds number boundary layer at Mach 2.9 showed that this quantity is not very sensitive to compressibility (see Figure 8.32). This result was confirmed by Cogne et al. (1993), who measured convection velocities directly using double-pulsed Rayleigh scattering flow visualization (see Figure 1.19). This implies that smaller space scales are found in supersonic flows. In contrast, the transverse scales related to turbulent diffusion remain unchanged, and the longitudinal scales determined from u' decrease. Now Spina and Smits (1987) showed that the direction of the maximum space-time correlation in their boundary layer at Mach 2.9 is steeper than at low speeds (see Figures 8.35 and 8.36), so that the streamwise correlation lengths are expected to decrease. As noted earlier,

this purely geometric explanation is not sufficient to explain all the evolution observed in Figure 8.43.

It is expected that the observed modifications in the flow structure and scales are due to compressibility. A possible interpretation can be found in the changes in the potential field induced in the external flow by the boundary layer, and in the generation of acoustic noise by supersonic boundary layers. Can they create smaller scales, and modify the orientation of the lines of maximum correlations? The variation of the angle was interpreted in the previous paragraph as a change in the direction of vortical structures. In fact, the two-point measurements by Spina and Smits did not use conditional statistics, and therefore did not discriminate between the vortical and potential contributions in the intermittent zone. In supersonic flows, the induced pressure field can depend on local conditions (the pressure perturbation induced by a large-scale structure, for instance), but also by the noise radiated by Mach waves. These waves can have low levels of $(\rho u)'$, but they are generally more conservative than ordinary turbulence, and could modify the space-time correlations for large separation distances. The formation of these Mach waves necessitates the velocity difference between the sources and the external flow to be supersonic. In a boundary layer, this condition is always fulfilled, but at moderate supersonic Mach numbers the part of the layer able to radiate Mach waves is very thin and generally confined to the viscous sublayer or the logarithmic zone. In this case, the behavior will be Reynolds and Mach number dependent. The orientation of the Mach waves will depend on this Mach number difference. For example, transonic perturbations would be very steep, and would help to make the maximum space-time correlation locus more vertical.

Another element, as noted by Laufer (1961), is an increase in the radiated field near Mach 3, which could be interpreted as follows. The convection velocity of the large eddies in the logarithmic layer is typically $0.8U_e$, regardless of the Mach number, and so the velocity difference with respect to the external flow is $0.2U_e$. Now, it may be expected that these eddies will start forming eddy shocklets when this relative Mach number is larger than, say, 0.6. This corresponds to an external Mach number of 3, and this criterion would be independent of the Reynolds number because the convection velocity of the large structures appears to be independent of Reynolds number. The measurements taken at a Mach number of 2.9 would then be near the onset of a new regime, and represent the first manifestation, in boundary layers, of compressible turbulence phenomena as observed in mixing layers. Such an interpretation, although speculative in many respects, is tempting because it can explain changes in the structure of u', as long as the radiated noise does not significantly affect the shear stress.

To conclude this section, the spectral data show that there are modifications to the motions which contribute to the energy scales but not to the turbulent transport. This implies that the primary action of compressibility

is to alter inactive motions. As these motions are related to the irrotational part of the fluctuations and to the pressure fluctuations induced by the layer, this explanation may be correct, but a full assessment would require a more complete knowledge of the two-point correlations and conditional statistics of turbulence in these flows.

8.7 Eddy Models of Turbulence

Eddies and coherent structures, particularly their interactions, are an integral part of our understanding of turbulence. Statistical descriptions, however, including correlations and ensemble averages, provide little information on eddy formation, growth, interaction, and dissipation. In this section, we describe some of the prevailing notions that form eddy models of turbulence.

The first physical model of the large-scale structure of turbulent boundary layers was proposed by Theodorsen (1955), who suggested that the basic structure of all turbulent shear flows is the inclined horseshoe vortex, as shown in Figure 8.44. Using the vorticity transport equation, Theodorsen attempted to prove that the only vortical structures which can sustain a nondecaying turbulent field must have a horseshoe shape. As seen in Figure 8.44, the model can certainly account for the generation of Reynolds stress. Between the legs of the vortex, the induced velocity ejects low-speed fluid up, away from the wall, into a region of higher mean velocity, hence $u' < 0$ and $v' > 0$ (a Quadrant II event). On the outboard sides of the legs, high-speed fluid is swept towards the wall, hence $u' > 0$ and $v' < 0$ (a Quadrant IV event).

The flow visualizations by Head and Bandyopadhyay (1981) provide strong support for the concept that at least some of the LSMs are loop-shaped vortical structures, with an aspect ratio that is Reynolds number dependent. Figure 8.45 shows that at $Re_\theta = 600$ the structures have the proposed horseshoe shape, and as Re_θ increases, the structures become elongated and appear more as hairpins. At all Reynolds numbers, the spacing between the legs of the structures is similar to the spacing between the near-wall streaks ($\approx 100\nu/u_\tau$). Note that Smith et al. (1991) and Smith and Walker (1997) present convincing arguments that the low-speed streaks are in fact artifacts of the passage of symmetric and asymmetric hairpin vortices. Head and Bandyopadhyay proposed that the loops extend to the wall, in support of Townsend's (1956) attached eddy hypothesis, although the Reynolds number dependence of their aspect ratio contradicts his Reynolds number similarity hypothesis.

Head and Bandyopadhyay (1981) further suggested that at low Reynolds numbers the LSMs were merely single horseshoe elements, but at higher Reynolds numbers the LSMs were actually agglomerations of many elongated hairpin vortices. They observed the generation of multiple hairpin loops in packets, where the heads of the loops lie along a line that is inclined to the wall at an angle of about 20°, as shown in Figure 8.46.

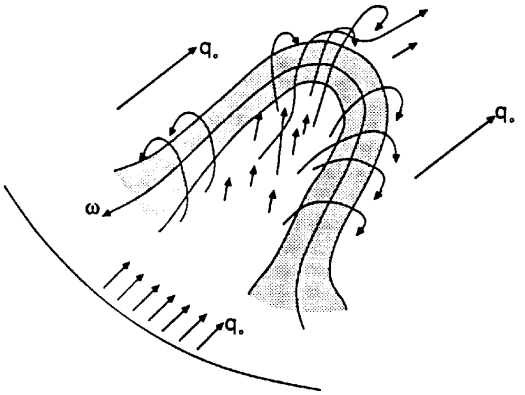

Figure 8.44. The horseshoe vortex proposed by Theodorsen (1955) as the basic structure in wall-bounded turbulent flows. (Figure from Spina (1988), with the author's permission.)

MacAulay and Gartshore (1991) also noted different structure angles using cross-correlations and conditional sampling. They determined that the major contributions to the broadband cross-correlations in a turbulent boundary layer at $Re_\theta = 8390$ came from δ-scale segments of the velocity signals, which encompass many aspects of the flow structure, rather than from individual hairpin eddies, which are an order of magnitude smaller than δ in the streamwise and spanwise directions at this Reynolds number. Using conditional sampling, they were able to measure the inclination angle of the sharp interface at the backs of the large-scale motions. This interface angle is compared to their measurements of the broadband structure angle in Figure 8.47, and the differences are significant.

Work by Zhou et al. (1997, 1999), Liu et al. (2001), and Adrian et al. (2000) has provided insight on the generation of coherent hairpin vortex packets containing a multiplicity of spatially organized hairpinlike vortices in channel and boundary layer flows, confirming and extending Head and Bapadhyay's observations using numerical simulations and PIV experiments. An elegant conceptual model of nested packets of hairpins (or fragments thereof) growing from the wall was developed. This model is illustrated in Figure 8.48. The resulting hierarchy of motions, with changes of scale as a result of vortex pairing, is in the same spirit as the mechanism of wall turbulence proposed by Perry and Chong (1982). Strong confirmation of the statistical significance of coherent hairpin packets has been provided by Marušić (2001) and Christensen and Adrian (2001). Of particular interest is the observation by Adrian et al. (2000) that at low Reynolds number, such packets contain two to three vortices, and that the number of vortices and the range of scales present increases

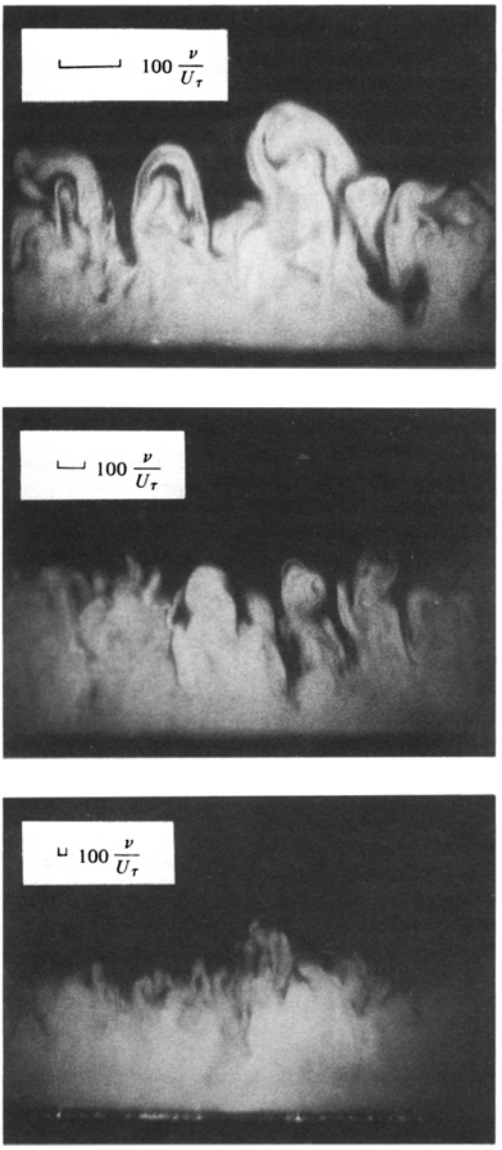

Figure 8.45. Flow visualizations by Head and Bandyopadhyay (1981), showing the Reynolds number dependence of vortex loop structures in a turbulent boundary layer. The visualizations were obtained by filling the boundary layer with smoke, and illuminating the flow with a laser sheet inclined 45° downstream. (a) $Re_\theta = 600$; (b) $Re_\theta = 1700$; (c) $Re_\theta = 9400$. (Figure from Head and Bandyopadhyay (1981).)

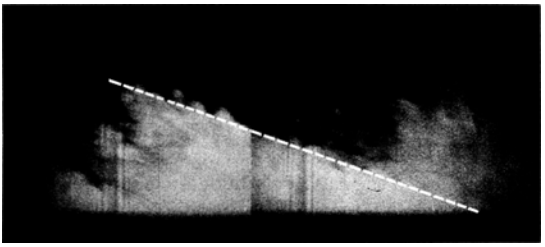

Figure 8.46. Example of 20° interface at R_θ = 17,500. Flow is from right to left. (Figure from Head and Bandyopadhyay (1981). Copyright 1981, Cambridge University Press. Reprinted with permission.)

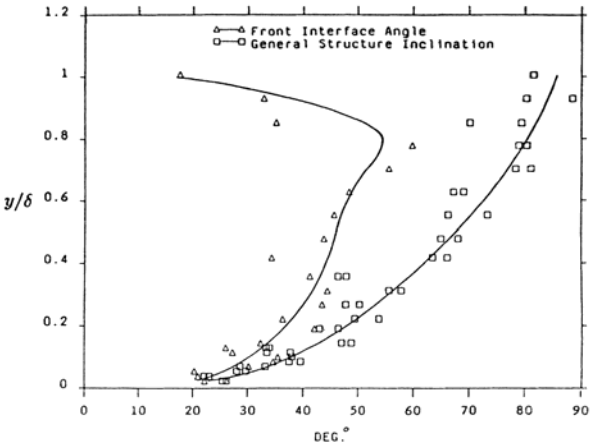

Figure 8.47. Structure angles measured by MacAulay and Gartshore (1991) in a turbulent boundary layer at Re_θ = 8390: □, broadband general structure angle; △, structure angle of the trailing (upstream) interface of the large-scale motions as detected using the VITA technique. (Figure from MacAulay and Gartshore (1991), with the authors' permission.)

with increasing Reynolds numbers.

At low Reynolds numbers, Head and Bandyopadhyay found that the LSMs exhibited a "brisk" overturning motion, and at higher Reynolds numbers they overturned slowly. This suggests that entrainment decreases with increasing Reynolds number, which is in agreement with the observation that the boundary layer grows more slowly with increasing Reynolds number. MacAulay and Gartshore (1991) proposed that at low Reynolds numbers, the horseshoe vortices are of the same magnitude as the boundary layer thickness in the spanwise and wall-normal directions. At high Reynolds numbers, the spanwise

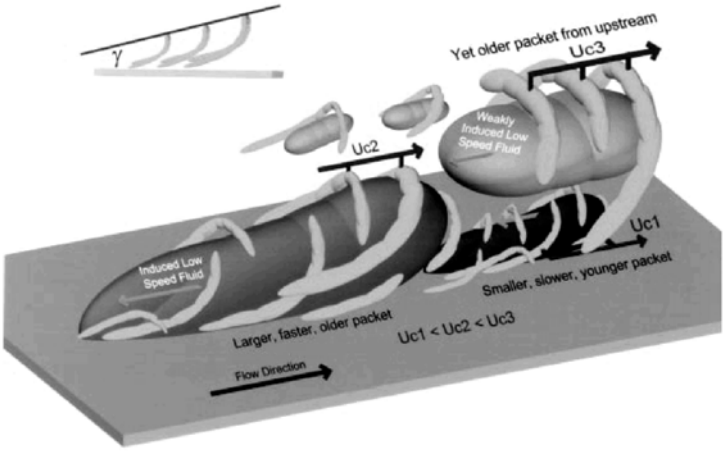

Figure 8.48. Conceptual model of hairpin packets and their evolution. (Figure from Adrian et al. (2000). Copyright 2000, Cambridge University Press. Reprinted with permission.)

scale of the hairpin eddies is much smaller than the boundary layer thickness. Due to their own self-induction, the hairpin vortices will propagate backwards (in a frame of reference moving at the mean velocity) through the low-speed fluid within the turbulent bulges. When they reach the back of a bulge, they encounter a sudden increase in streamwise velocity that balances their self-induced velocity. MacAulay and Gartshore suggest that stronger structures (with higher self-induced velocities) will penetrate the rear interface farther than weaker structures. This results in the appearance of small-scale structures on the backs of the large-scale motions, similar to Falco's typical eddies (see next section). They suggested, in fact, that Falco's eddies may simply be the heads of the hairpin vortices. When the hairpin vortices cease their backward propagation, their self-induction will continue to carry them up, away from the wall, resulting in a slow overturning motion.

8.7.1 Inner-Outer Interactions

Sreenivasan and Sahay (1997) describe the Reynolds number dependence of the peak of the Reynolds shear stress in its location (y_p^+) and maximum value. Combined with the Reynolds number dependence of the peak in the streamwise turbulence intensity (Fernholz and Finley, 1996), these observations indicate that the near-wall region is not entirely independent of the outer layer dynamics. Morrison et al. (2004) and Zhao (2005) have revisited the long-standing notion of active and inactive motions, and they provide compelling evidence to show that the local scaling behavior in fully developed pipe flow is determined

both by inner and outer layer motions. The uncertainty regarding the scaling of the bursting frequency also illustrates the problem.

To this end, Delo and Smits (1997) and Delo et al. (2004) obtained time resolved three-dimensional visualizations of the scalar field in a boundary layer at $Re_\theta = 701$. They noted that groups of the large-scale motions were frequently assembled into agglomerations measuring up to 5δ in length, and suggests that the agglomerations are formed through the merging of adjacent, previously existing individual vortical structures as they convect downstream. Some evidence was found that the large agglomerations actively "build" themselves as they convect downstream, through the addition of near-wall fluid. Most of the ejection events identified in a spatial distribution occurred simultaneously, soon after the passage of the extended, large-scale structures. The fluid ejected by these events generally penetrated through the trailing edges of the structures, growing like Head and Bandyopadhyay's hairpin packets, effectively increasing their streamwise extent. It was tentatively proposed that the addition of energetic near-wall fluid in this manner serves to perpetuate the active nature of the large-scale structures. The structures appear to be "long" enough so that after perturbing the inner layer low-speed streaks and triggering an ejection, the trailing edges of the structures are still in the neighborhood to profit from the addition of the ejected near-wall fluid.

Another example, concerning the relationship between the large-scale motion and the wall shear stress at much higher Reynolds numbers, was given by Brown and Thomas (1977). They found that the large-scale motions were inclined at an angle of 18° to the wall and extended about 2δ in the streamwise direction, similar to Head and Banyopadhyay's observations on hairpin packets. As the structures passed over the wall, they created a characteristic wall shear stress signature. Brown and Thomas suggested that this wall shear stress pattern was related to the bursting process, and concluded that the large-scale, outer layer structure influenced the near-wall structure and dynamics. They found that the results were independent of Reynolds numbers when scaled on outer variables, for $R_\theta = 4940$ and 10,160.

In addition, the flow visualizations by Falco (1977) showed that there may be at least two types of organized motions in the outer layer: LSMs and "typical eddies" (see also Klewicki (1997)). He found that the typical eddies are small-scale motions, which scale on wall variables and are responsible for a significant fraction of the total Reynolds shear stress in the outer layer. The average streamwise extent of the LSMs was about 1.6δ at $R_\theta \approx 1000$. The streamwise length scale of the typical eddies had a constant value of about $200\nu/u_\tau$ for $1000 < R_\theta < 10{,}000$. The vertical length scale varied nearly linearly from $100\nu/u_\tau$ to $150\nu/u_\tau$ over the same range of Reynolds numbers. Falco found that the typical eddies generally appear on the backs of the LSMs, and propagate towards the wall, thus acting as sweeps very near the wall (see Figure 8.49). Cantwell (1981) called these intense small-scale motions

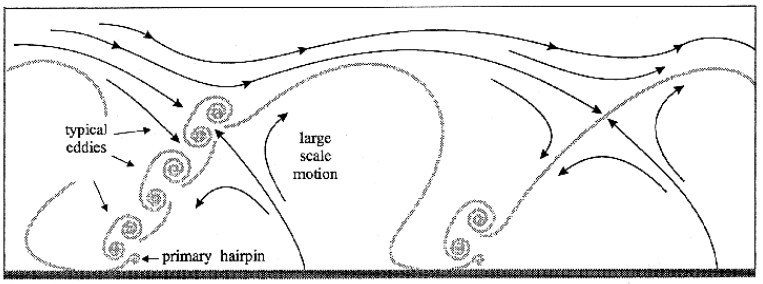

Figure 8.49. Schematic representation of typical eddies grouped on the back of a large-scale motion. (Figure from Falco (1991). Copyright 1991, The Royal Society. Reprinted with permission.)

"energetic outer-flow eddies".

Falco claimed that the typical eddies may be an intermediate link between the inner and outer layers. As discussed by Smith and Smits (1991b), however, if the typical eddies scale on wall variables then at very high Reynolds number, where δ^+ is very large, the typical eddies will become vanishingly small compared to the boundary layer thickness, and they are unlikely to be dynamically significant (that is, they will not carry significant levels of shear stress). Furthermore, flow visualizations at very high Reynolds numbers show features that appear to be very similar to the typical eddies observed by Falco at lower Reynolds numbers, but which are at least an order of magnitude larger (in terms of inner variables), even when the variations in fluid properties, as expressed by the difference between R_θ and R_{δ_2}, are taken into account.

8.7.2 Summary of Boundary Layer Eddy Structure

Here, we describe a unified picture of boundary layer eddy structure that attempts to represent the important kinematic and dynamic behavior in wall-bounded turbulent flows. It is based in large part on the model suggested by Smith and Walker (1997).

The dynamic process of turbulence production and the formation of structure is described as a cycle that begins with the growth of a low-speed streak. The growth continues until the passage of a disturbance of sufficient size and strength impresses a local adverse pressure gradient on the streak causing a local deceleration. This deceleration creates a three-dimensional inflectional profile at the interface between the streak and the higher speed flow in the wall region. The region above the streak is unstable to small local disturbances, and oscillations begin on the top of the streak. The three-dimensional sheet of vorticity above the streak will develop waves due to the oscillations, roll

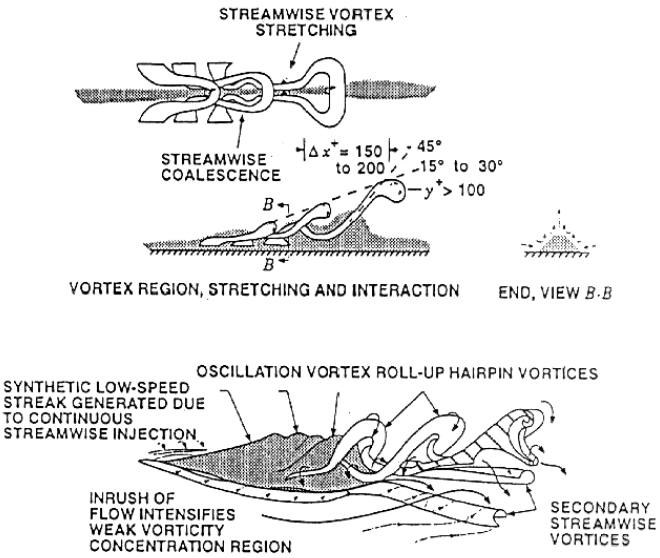

Figure 8.50. Top: Illustration of the breakdown and formation of hairpin loops during a streak-bursting process. Low-speed streak regions are indicated by shading. Bottom: Schematic of breakup of a synthetic low-speed streak generating hairpin vortices. Secondary streamwise vortical structures are generated owing to the inrush of fluid. (From Acarlar and Smith (1987a), with permission.)

up, and concentrate the vorticity in locations on the sheet. This process takes place at a y^+ of between 15 and 20, and there can be between two and five concentrations per streak.

As the roll-up continues, the vortices begin to look like horseshoe vortices (see Figure 8.50). Biot-Savart interactions between various portions of the vortex amplify the distortion. Self-induced movement away from the wall occurs and the vortex is stretched by the steep mean velocity gradient. Legs of the horseshoe, which are a pair of counterrotating vortices oriented in the streamwise direction, develop as the loop is stretched. As the vortex becomes elongated, it begins to look more like a hairpin vortex and the vorticity is increased. The legs tend to pump low momentum fluid away from the wall and thereby perpetuate the low-speed streak. The head or arch creates a streamwise pressure gradient that will cause the liftup and ejection of low-momentum fluid from the low-speed streak as it moves downstream. As the process proceeds, the hairpin continues to be stretched and the head moves farther away from the wall due to self-induction.

As the loops are dragged over the viscous layer near the wall, they help

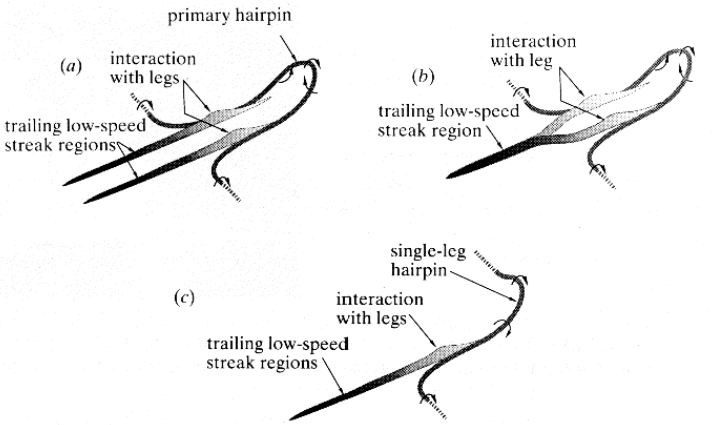

Figure 8.51. Schematic illustrating how advecting symmetric and asymmetric hairpinlike vortices generate low-speed streaks. (Figure from Smith et al. (1991). Copyright 1991, The Royal Society. Reprinted with permission.)

to regenerate new vortices through an interaction with the viscous wall layer (Figure 8.51). The passage of successive loops can tend to focus the streak so that it can continue to grow, or buffet it to weaken it. In either case, the impingement of subsequent vortices creates the appearance of waviness and swaying, a commonly observed behavior.

The timing on the formation of the loops out of the sublayer material appears to be such that as they rise they form the backs of the LSMs, creating a very active shear layer out of the conjunction of the heads of the vortex loops (see also MacAulay and Gartshore (1991), Bernard and Wallace (1997), and Adrian et al. (1998)). The hairpins often align themselves so that their heads lie along a line forming a 15° to 30° angle with the wall, whereas the individual hairpins make an angle of about 45°.

The stretching of the vortex loops by the surrounding flow (viewed either as a background mean velocity gradient, or the summation of the velocity induced by all surrounding vortex loops) requires work to be done. Also, the narrowing of the vortex tube making up the loop will increase the velocity gradients inside the tube, increasing its dissipation rate as the square of the gradients. This dissipation will be greatest near the wall where the velocity gradients are strongest, and diminish in the outer flow where the gradients are relatively weak. According to Smith and Walker (1997):

> ... the process of growth to larger scales in a fully-turbulent boundary layer can be explained by the proximity of multiple hairpin-like vortices in different phases of development, which creates a condition

> conducive to coalescence, or three-dimensional vortex amalgamation. This amalgamation process ... suggest(s) that local collections of hairpin vortices can intertwine and interact to yield essentially a hairpin-like structure of somewhat larger scale... This clearly suggests that the outer region of a turbulent boundary layer can evolve from hairpin vortex structures and that the large, arch-type vortices (Robinson, 1991a) and rollers (Falco, 1977) observed in the outer-region structures directly interface with the freestream flow. The overturning of the structures plays an instrumental part in inducing the flow of higher-speed fluid toward the wall (i.e., intermittent engulfment), which eventually finds its way to the wall along a complex gauntlet of vortex-induced motions, terminating in a "sweep" motion at the wall... However despite the overall size and strength of the outer structures, the stretching mechanism for energy transfer to these larger-scale vortical structures is strongly diminished because of the weak mean velocity gradient in the outer region. Following an initially strong energy input to the initial vortex scales near the wall, these outer structures will basically "evolve" to larger and larger scales, but with no significant additional energy input, eventually succumbing to slow, viscous dissipation. The outer part of the boundary layer of the boundary layer may thus be regarded as a "graveyard" for vorticity, where the cumulative remnants of deformed wall-region vortices pass through a complicated process of dissipation, diffusion and mutual cancellation, similar to the model of Perry and Chong (1982) (Figure 8.52).

We note, however, that the heads of the hairpin loops, being a localized concentration of shear stress, continue to be an active feature of the LSMs. In addition, the viscous diffusion of the legs may free the heads to form vortex loops or rings, with at least two consequences. First, the outer layer motions are no longer attached to the wall, and will look more like that shown in Figure 8.48. Second, at least some of the vortex loops may have an induced velocity that directs them to the wall, as typical eddies (Klewicki, 1997). As the Reynolds number increases, there need to be other levels of organization where very large scale motions emerge because the active motions seen on the backs of the LSM's have a typical dimension of 200 wall units, and these size motions cannot continue to be important in the shear stress budget since the stress in the outer layer scales with outer layer variables. Smits et al. (1989) proposed that as the Reynolds number increases the number of discrete scales of motion also increase. At the lowest Reynolds numbers ($1000 < R_\theta$ and $\delta^+ < 500$), a single scale dominates. This scale must be the same as that of the typical eddy, because they are of the same order as the boundary layer thickness. At higher Reynolds numbers ($1000 < R_\theta < 5000$ and $500 < \delta^+ < 2500$), two scales appear: the large-scale outer layer bulges and Falco's typical eddies. The

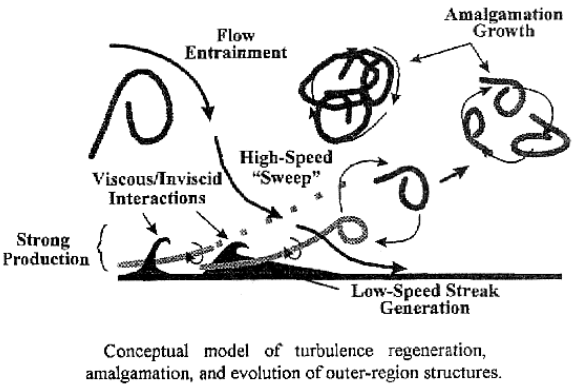

Figure 8.52. Conceptual model of turbulence regeneration, amalgamation, and evolution of outer-region structures. (Figure from Smith et al. (1991). Copyright 1991, The Royal Society. Reprinted with permission.)

typical eddies still make significant contributions to the Reynolds stresses. With a further increase in Reynolds number, the large-scale motions must carry more shear stress owing to the diminishing importance of the typical eddies (see also Murlis et al., 1982). It is possible that a third scale appears, corresponding to the smaller bulges seen at the edges of the large-scale bulges. Falco's typical eddies are now much smaller than the energy-containing range (which scales with δ), so that they are no longer dynamically important (with $Re_\theta = 35{,}000$, $200\nu_w/u_\tau$ corresponds to a frequency of about $100U_e/\delta$). It may be expected that the third scale would scale on outer layer variables, although some form of mixed scaling may also be appropriate. The appearance of new scales with increasing Reynolds numbers at approximately equal intervals in $\log \delta^+$ should be reflected in the behavior of the turbulence, especially the higher-order moments. At present there are insufficient data to support these proposals.

Finally, we address the question of symmetric and asymmetric vortex loops. The horseshoe vortex of Theodorsen (1955), the hairpin loops of Head and Bandyopadhyay (1981), and the Λ-shaped vortices of Perry and Chong (1982), are symmetric structures. It has been widely reported in experimental studies and DNS that the vortex structures observed in boundary layers are only rarely symmetric and asymmetric structures dominate (see, for example, Kline and Robinson (1989) and Kline and Portela (1997)). In the three-dimensional visualizations by Delo et al. (2004), symmetrical structures are rarely seen, although it is readily apparent that legs and arches are always part of the same vortex looplike structure. However, as argued persuasively by Smith and Walker (1997), any kinematic description of the near-wall cycle in terms

of symmetric structures can equally be cast in terms of asymmetric events (see also Figure 8.51). The important point is the sequence of events and their underlying mechanisms, and because the presence of asymmetry does not seem to affect the underlying physics, symmetrical models can be used for simplicity.

8.8 Final Remarks

From our consideration of subsonic flows it appears that, in contrast to the mean flow behavior, the turbulent stresses do not necessarily follow the inner/outer scaling arguments. For example, as found previously by Sreenivasan (1989) and Gad-el-Hak and Bandyopadhyay (1994), the Reynolds number can have a significant effect on the level of the maximum stress, and the location of that maximum in the boundary layer. In other respects, the scaling arguments put forward by Perry and his co-workers (see, for example, Perry and Li (1990)) indicate how the stresses may scale in the overlap region, and the experimental evidence tends to support their arguments, although their proposed constants may need to be adjusted somewhat.

The evolution of the organized motions in the boundary layer also depends on Reynolds number. In particular, the streamwise scaling of the outer layer structure is rather sensitive, where the scale increases with Reynolds number. This was confirmed by direct measurements of the space-time correlations and spectra. In contrast, the spanwise scaling appears to be insensitive to Reynolds number, so that on average the structures become more elongated in the streamwise direction with increasing Reynolds number. The average inclination of the outer layer structures also decreases, which may be related to the increase in the streamwise aspect ratio. It also appears that the spanwise scaling of the sublayer streaks is fixed at a mean value of about $100\nu/u_\tau$ over a very wide Reynolds number range, although the trend with Mach number is unknown.

For supersonic flows with moderate Mach number, it seems that the direct effects of compressibility on wall turbulence are rather small, as was found for the mean velocity distribution. Again, the most notable differences between subsonic and supersonic boundary layers may be attributed to the variation in fluid properties across the layer. Under the assumption that the length scales are not affected by compressibility, the turbulent stresses in the outer region scale on the wall stress, as first suggested by Morkovin (1962), as far as we can tell from the available data. This result is not surprising in some ways because the fluctuating Mach number ($M' = M - \overline{M}$) for moderately supersonic flows is considerably less than one, as illustrated in Figure 7.1.

However, a more detailed inspection of the turbulence properties reveals certain characteristics that cannot be collapsed by a simple density scaling.

For example, the shear correlation coefficient R_{uv} decreases with distance

from the wall in some supersonic flows instead of remaining approximately constant as in subsonic flows. There are other results, however, which indicate that R_{uv} follows the incompressible trend, and there is the possibility that the differences may be caused by a Reynolds number rather than a Mach number dependence. Unfortunately the database is very sparse, and considerable further effort is needed before these issues can be laid to rest. With respect to the streamwise and spanwise length scales of the large-scale motions, and their average inclination to the wall, the effect of Mach number is clear. Even if we account for the change in time scale of the energy-containing eddies Λ/u', we see that the lateral correlations are almost unaffected by changes in Mach and Reynolds number. The streamwise length scales are reduced significantly by increasing Mach number, and the angle of inclination is increased, although in coming to these conclusions we have implicitly assumed that Mach and Reynolds number effects are independent. It is necessary to make this assumption because the data do not overlap to any significant extent, and we are forced to compare experiments in supersonic flow with the results obtained in subsonic flow, usually at a different Reynolds number. In fact, the actual Reynolds number to be used in such a comparison is controversial because there is usually a major difference between the values of Re_θ and $R_{\delta 2}$. Finally, there is an order-of-magnitude decrease in the rate of decay of the large-scale motions as the Mach number increases from low subsonic to high supersonic values (Smits et al., 1989).

How can we explain these differences? Part of the answer may lie in understanding the role of Reynolds number more clearly, but understanding the effects of fluid property variations may be more important. In that respect, we need more direct numerical simulations and more detailed turbulence measurements at higher Mach numbers. We are seeing subtle differences at supersonic speeds that may signal the onset of direct compressibility effects such as the increased importance of pressure fluctuations and pressure-velocity correlations. These effects will become more obvious at hypersonic Mach numbers, and such studies will undoubtedly contribute to our understanding of the supersonic behavior.

Although few specifics are known, the turbulence physics become more complex as the Mach number increases beyond about five. For example, the Strong Reynolds Analogy and Morkovin's hypothesis are staples of boundary layer analysis at moderate Mach number. However, an upper Mach number limit must exist on the applicability of these simplifying assumptions, if only because there is a limit on the magnitude of temperature fluctuations. For instance, the SRA indicates that the standard deviation of the temperature fluctuations becomes comparable to the mean temperature at Mach numbers as low as 5. Indeed, the change in magnitude of the fluctuating Mach number distribution as the flow enters the hypersonic range (see Figure 7.1) points to the possibility of a dramatic alteration of turbulence dynamics due to com-

pressibility effects around Mach 5 (in comparison, the turbulence Mach number M_t is less than 0.3 even for the Mach 7.2 and 9.4 flows). Unlike the distribution of M_t, the fluctuating Mach number develops a peak near the middle of the boundary layer where both the velocity and temperature fluctuations are important. This behavior, when considered together with the large gradients in density and viscosity near the wall, also leads to the conclusion that there may be substantial differences in turbulence dynamics at higher Mach numbers.

At the same time, the near-wall gradients in density and viscosity are strongly dependent on heat transfer, and therefore the thickness of the sublayer will depend on Mach number, Reynolds number, and wall temperature. This raises the issue of how the viscous instability of the sublayer changes when fluid properties vary with distance from the wall (Morkovin, 1992). Because the local Reynolds number increases away from an adiabatic wall faster in supersonic flow than in incompressible flow, we would expect the flow to become less stable as we move away from the wall at a rate that is faster than in an incompressible flow at the same friction velocity. The effect on the near-wall stability and the bursting process in supersonic flows is not clear, but DNS may well provide the answer in the near future.